

CZECH TECHNICAL UNIVERSITY IN PRAGUE

Faculty of Civil Engineering
Experimental Centre

DIPLOMA THESIS

**Complex analysis of a prestressed concrete
girder with GFRP reinforcement subjected
to freeze/thaw cycles**

MICHAL HLOBIL

Supervisor: Ing. Radoslav Sovják, Ph.D.
Prague, December 2011

Zde vložit zadání diplomové práce

Statement

I hereby confirm that I have worked on this diploma thesis on my own just with the methodical support of my supervisor Ing. Radoslav Sovják, Ph.D.

In addition I declare that all the references I have used to prepare this thesis are stated in the bibliography.

In Prague 15th December 2011

.....

Michal Hlobil

Acknowledgement

First and foremost I would like to thank my supervisor, Ing. Radoslav Sovják Ph.D., for his help, enthusiasm and support not only during my last semester, but since the moment I met him. I cannot forget to thank Ing. Tomáš Krejčí, Ph.D. for his help with modeling of heat transport in TRFEL software. The collective team of the Experimental centre deserve my thanks for helping me with the experimental part of this thesis. Also I would like to thank those, whom I accidently didn't mention here. But you know, who you are.

Last but not least, I would like to thank my parents for their support during my entire studies.

Abstract

Bond between reinforcement and concrete is formed when cement paste shrinks around the reinforcement during the hardening phase. Bond strength is essential for the reinforcement to be effective in concrete as it ensures and provides transfer of strain between the two materials. It depends on the interlocking of a hardened surface of the reinforcement with the cement matrix, thickness of concrete layer surrounding the reinforcement and similar thermal expansion of both materials.

This thesis presents numerical simulations and experimental results from testing of bond strength between nonmetallic GFRP reinforcement and concrete. Two groups of samples were fabricated using air entrained concrete. Prestressed GFRP rebars were used to reinforce 1,8 m long concrete beams. The first group was cast without shear reinforcement and the second group with it. After 28 days of curing part of the beams from group 1 were subjected to freeze/thaw cycles with temperatures ranging from 40 °C to -30 °C for 50 days. The second group was loaded with a modified temperature cycle for 75 days. Then all beams were subjected to a four point bending test and their results compared with reference beams.

Results indicate that quality of concrete was not deteriorated by freeze/thaw cycles. Ultimate load bearing capacity of all beams remained very similar. Beams from group 1 (without shear reinforcement) behaved as if the prestressing force remained until testing regardless whether the beams were subjected to freeze/thaw cycles or not. Beams from group 2 (with shear reinforcement) behaved as if the prestressing force was lost – their cracking moment was reduced to almost 50 % as a numerical model in ATENA software predicted. This was anticipated for beams subjected to prolonged freeze/thaw cycles for 75 days. But why the reference beams lost all prestressing force and behaved as beams under freeze/thaw cycles remains unknown.

Keywords: Bond; Concrete; Freeze/Thaw Cycle; GFRP; Prestressing

Abstrakt

Spolupůsobení mezi výztuží a betonem se vytváří při smršťování cementové pasty okolo výztuže během fáze tvrdnutí. Soudržnost je nezbytná pro to, aby výztuž v betonu působila efektivně, neboť zajišťuje stejné přetvoření a přenos napětí mezi oběma materiály. Závisí na drsnosti povrchové úpravy prutu výztuže, tloušťce krycí vrstvy betonu a teplotní roztažnosti obou materiálů.

Tato práce předkládá výsledky numerických simulací a provedených experimentů za účelem testování soudržnosti mezi nekovovou GFRP výztuží a betonem. Dvě skupiny vzorků byly zhotoveny z provzdušněného betonu. Betonové trámy 1,8 m dlouhé byly vyztuženy jedním předepnutým prutem GFRP výztuže. Trámy z první skupiny vzorků neobsahovaly smykovou výztuž, zatímco trámy z druhé skupiny ano. Po 28 dnech ošetřování byly trámy z první skupiny zatíženy teplotním cyklem v rozmezí od 40 °C do -30 °C po dobu 50ti dnů. Trámy z druhé skupiny vzorků byly zatíženy upraveným teplotním cyklem po dobu 75ti dnů. Všechny trámy včetně referenčních z obou skupin byly následně podrobeny zkoušce na čtyřbodový ohyb a jejich výsledky vzájemně porovnány.

Výsledky naznačují, že kvalita betonu nebyla teplotními cykly nijak narušena. Výsledná ohybová únosnost všech trámů byla téměř porovnatelná. Trámy z první skupiny (bez smykové výztuže) se chovaly jako kdyby předpínací síla nepoklesla, a to ani u referenčních, ani u trámů vystavených teplotnímu zatěžování. Trámy ze druhé skupiny (obsahující smykovou výztuž) se chovaly tak, jako kdyby došlo k úplné ztrátě předpětí – ohybový moment při vzniku trhlin byl nižší téměř o 50 %. Tento výsledek odpovídal předpovědi numerické analýzy provedené v programu ATENA. Toto bylo očekávané pro trámy vystavené upravenému teplotnímu zatěžování, které trvalo 75 dní. Proč se ale předpínací síla vytratila i z referenčních trámů zůstává i nadále nevysvětleno.

Klíčová slova: beton; GFRP; předpínání; soudržnost; zmrazovací/rozmrazovací cykly

Notation and abbreviations

RC	reinforced concrete
Rebar	reinforcing bar
FRP	fibre reinforced polymer
GFRP	glass fibre reinforced polymer
CFRP	carbon fibre reinforced polymer
AFRP	aramid fibre reinforced polymer
CTE	coefficient of thermal expansion
F/T	freeze/thaw
LCC	life cycle cost(s)
FVF	fibre volume fraction
RVF	resin volume fraction
PMC	polymer matrix composite
MMC	metal matrix composite
CMC	ceramic matrix composite

Contents

1	Introduction	1
1.1	Motivation	2
1.2	Aim of the work	3
1.3	Scope of the work	4
2	State of the art	5
2.1	Structure of FRP	5
2.2	Fibres	7
2.2.1	Glass fibres	8
2.2.2	Carbon fibres	9
2.2.3	Aramid fibres	12
2.3	Matrix	16
2.3.1	Thermosetting resins	16
2.3.2	Thermoplastic resins	18
2.4	Fabrication process	19
2.5	Features of FRP composites	20
2.6	Mechanical properties of FRP	22
2.7	Thermal properties of FRP	24
2.8	Durability under freeze/thaw cycles	25
3	Numerical approach	28
3.1	Micromechanical analysis of a lamina	28
3.1.1	Basic properties	29
3.1.2	Strength of material approach	31
3.1.3	Semi-empirical approach by Halpin–Tsai	37
3.1.4	Mori–Tanaka approach	39
3.1.5	Comparison of results	40
3.2	Modeling of heat transfer in MATLAB	42
3.2.1	Non-stationary heat transfer	42
3.2.2	Implementation in MATLAB	44
3.2.3	Results of heat transfer modeling	46

3.3	Nonlinear analysis in ATENA	48
3.3.1	Model generation	49
3.3.2	Solution method for numerical analysis	51
3.3.3	Results from numerical analysis	52
4	Experimental approach	54
4.1	Design of specimens	54
4.2	Prestressing composite rebars	55
4.3	Production of samples	57
4.4	Freeze/thaw cycles	60
4.5	Testing of specimens	62
4.5.1	Determination of air content	62
4.5.2	Verification of temperature	64
4.5.3	Compressive strength of concrete	65
4.5.4	Tensile strength of concrete	68
4.5.5	Four-point bending test	70
5	Conclusion and further research	77
5.1	Resume from numerical modeling	77
5.1.1	Micromechanical analysis of a lamina	77
5.1.2	Modeling of heat transport	78
5.1.3	Nonlinear analysis in ATENA	78
5.2	Resume from experimental approach	78
5.3	Suggestions for further research	80

List of Tables

2.1	Chemical composition of glasses	10
2.2	Typical properties of glass fibres	10
2.3	Typical properties of carbon and aramid fibres	15
2.4	Typical properties of thermosetting matrixes	18
2.5	Typical properties of thermoplastic matrixes	18
2.6	Typical properties FRP, steel and concrete	24
3.1	Material properties of GFRP constituents	40
3.2	Calculated resultant properties of the composite rebar	41
3.3	Input parameters for MATLAB	45
3.4	Results from ATENA	53
4.1	Overview of specimens	55
4.2	Reinforcement properties	56
4.3	Prestressing force	58
4.4	Concrete mixture	58
4.5	Overview of freeze/thaw cycles	61
4.6	Measured air content	64
4.7	Placement of thermometers in beams PGB 7–8	64
4.8	Compressive strength of samples from group 1 subjected to F/T cycles	67
4.9	Compressive strength of reference samples from group 1	67
4.10	Compressive strength of samples from group 2 subjected to F/T cycles	67
4.11	Compressive strength of reference samples from group 2	68
4.12	Overview of the mean values for all specimens	68
4.13	Tensile strength of reference samples from group 1	69
4.14	Tensile strength of samples from group 1 subjected to F/T cycles . . .	70
4.15	Tensile strength of samples from group 2 subjected to F/T cycles . . .	70
4.16	Tensile strength of reference samples from group 2	70
4.17	Overview of the mean values of tensile strength	71
4.18	Load bearing capacity of beams	75

List of Figures

2.1	Stress–strain diagram for glass fibres	10
2.2	Stress–strain diagram for carbon fibres	12
2.3	Stress–strain diagram for aramid fibres	14
2.4	Comparison of stress–strain diagrams for all fibres	14
2.5	Scheme of a pultrusion line	19
2.6	Stress-strain diagram for FRP	23
2.7	Comparison of stress-strain diagrams for steel and GFRP	24
3.1	Determining elastic modulus on RVE	32
3.2	Prescribed freeze/thaw cycle	45
3.3	Temperature field over the cross-section #1	46
3.4	Temperature field over the cross-section #2	47
3.5	Temperature field over the cross-section #3	47
3.6	Temperature at GFRP rebar during freeze/thaw cycle	48
3.7	Geometry of the model	49
3.8	Mesh on the model	51
3.9	Newton-Raphson iteration scheme	52
3.10	Results from ATENA	53
4.1	Geometry of concrete beams	54
4.2	Anchor at the end of the rebar	56
4.3	Close-up on the surface	56
4.4	Prestressing GFRP rebar	57
4.5	Close up on the steel anchor	57
4.6	Close up on HBM load cell	57
4.7	Placement of thermometers	58
4.8	Close-up on the thermometer	58
4.9	Freeze/thaw cycle within 24 hours	61
4.10	Freeze/thaw cycle within 36 hours	62
4.11	Air meter showing approximate air content	63
4.12	Measured temperature on the GFRP rebar	65
4.13	Measured temperature in the middle of the cross-section	65

4.14	Measured temperature on the outer surface	66
4.15	Test setup for compressive strength testing	66
4.16	Test setup for tensile strength testing	69
4.17	Test configuration	71
4.18	Results of beams from group 1	72
4.19	Results of beams from group 2	73
4.20	Collapsed beam by shear from group 1	73
4.21	Collapsed beam by bending from group 2	74
4.22	Results of all beams	76

Chapter 1

Introduction

Certain periods of time throughout human history were named after different materials which mankind used for their needs. Modern archeology divides the timeline into three main stages. The first described period is the *Stone Age*. Its origin cannot be exactly traced back in human history and neither can we designate its duration. Archeologists date the beginning of Stone Age 2,5 million years back judging from the remains of artifacts that can be found. Humans learned how to make their own tools and use them to their benefit for gathering food. This was a huge technological improvement as sharpened stones enabled them to hunt animals. These artifacts gave then the name to this age because most of them were of stone (and a minority of bones).

Tools that people used have further improved in time. Metal ores were discovered and by smelting them together new materials could be produced. A typical example are copper and tin ores. By smelting them a new material is created – bronze. This presented a huge step forward for mankind and it gave the name to this age. During *Bronz Age* people learned how to create objects much lighter than stone, yet sharper. But bronze tools had an important disadvantage – they were brittle. Bronze tools and weapons were traded between different regions. This business flourished due to the fact that not all regions had deposits of copper ore and wars were waged throughout the known world. Dating the Bronze Age is also very difficult but historians generally agree that it took place between 3300–1300 BC, depending on the region.

But is a brittle material sufficient for demanding applications? Definitely not. People began to understand the benefits of iron ore only after they fully mastered the smelting of bronze. Iron ore demanded higher temperatures to melt and also the right amount of carbon added to make steel. If the carbon content is on the one hand too low, than wrought iron is formed. It is ductile but cannot be treated with high temperatures. If the carbon content is too high on the other hand, iron becomes too brittle and too hard to be heat treated. But during the *Iron Age* people began to

master smelting iron alloys and their products quickly replaced bronze and became widespread throughout the known world. The use of steel penetrated into every part of the industry, not only for tools and weapons. Even today steel is used in many applications.

But evolution cannot be stopped. Steel may have served us well for centuries but the demand to build higher and stronger reached the limits of this material. Let us put steel aside and accept its successor. A new age calls for new materials – ones that will be stronger, lighter and more durable than steel. Take for example the new Airbus A380 – the biggest passenger aircraft constructed up to date. An aircraft so huge that if constructed using steel it would be too heavy to flight. Steel then had to be replaced with modern materials to save weight. The load bearing element of wings is made of carbon fibre reinforced polymers, while several important parts of wings use different composite materials such as glass fibre aluminium laminates. All this was developed with only one idea in mind – to make the structure strong as steel but at the same time much lighter and more durable. Now we are standing on the edge of a boom. A boom of materials designed with the requested properties. No longer do we have to accept that materials have their own properties and we have to figure out how to use them in an effective way. Today, we can design and produce materials with requested properties to suit our needs. Welcome to the new age – the *Composite Age*.

1.1 Motivation

The idea to improve properties of concrete in tension was developed by a French gardener Joseph Monier. He used steel rebars to reinforce flower pots in the 1850's. He patented this idea back in 1867 [1] and continued to improve his design further. Nowadays, the use of reinforced concrete is dominant for civil engineering structures. Concrete without reinforcement has only minor applications and is used only for inferior structures.

In order to make reinforcement effective in a concrete structure three main conditions apply [2]:

- *concrete cover* – according to the design codes, the reinforcement has to be embedded in concrete and protected from the outside environment by a sufficient cover. Its thickness depends on many factors such as the diameter of the rebar, the technology of fabrication (Eurocode [3] states that monolithic structures should have a thicker layer of concrete cover compared to prefabricated structures) and the outside environment.

- *ribs* – if the surface of the reinforcement contains ribs, they help to secure and improve bond between concrete and reinforcement.
- *thermal expansion* – steel and concrete have a fairly similar coefficient of thermal expansion – approximately $12 \cdot 10^{-6} \text{ K}^{-1}$.

Glass fibre reinforced polymer is, on the other hand, a transversely isotropic material. Its properties depend on the orientation of fibres and properties of the matrix. In the longitudinal direction (parallel to the orientation of fibres), the coefficient of thermal expansion depends mainly on fibres and is approximately $6 - 7 \cdot 10^{-6} \text{ K}^{-1}$. However, in the perpendicular direction, the coefficient is ruled by the matrix and depending on specific type, it can be up to $50 \cdot 10^{-6} \text{ K}^{-1}$, which is 4 times higher than concrete.

1.2 Aim of the work

Different coefficients of thermal expansion between GFRP reinforcement and concrete could pose a problem for civil engineering structures. During the day, temperature of the structure changes only by a few degrees. But a more important fluctuation occurs throughout the year as the seasons change. The difference between an average summer day (in July) and winter day (in January) [4] can be around $25 \text{ }^\circ\text{C}$. But that is on the average. When considering extremes, the temperature difference can be more than $60 \text{ }^\circ\text{C}$.

When thermal loading is applied the difference between coefficients of thermal expansion of GFRP and concrete causes GFRP to shrink and expand more than the surrounding concrete. This damages the bond between these two materials. And the lower the bond strength, the lower the capacity to transfer strain making the rebar less effective. And over time the capacity to transfer tensile stress is reduced along with the ultimate load bearing capacity of the reinforced member.

In order to find out how the load bearing capacity will be reduced, two groups of concrete beams prestressed with GFRP reinforcement were prepared. After casting they were cured in laboratory conditions for 28 days. The first group consisting of three 1,8 m long concrete beams was subjected to fifty freeze/thaw cycles with temperatures ranging from -30 to $+40 \text{ }^\circ\text{C}$. The second group contained two beams made using the same concrete mixture as the previous three beams. They were cured for the same time in laboratory conditions and afterwards they were subjected for 75 days to a modified freeze/thaw cycle. After thermal loading, all beams were subjected to a four-point bending test and the results were compared.

1.3 Scope of the work

This work consists of 5 chapters. The first chapter introduces the aim of this work along with a motivation for this thesis. A short historical overview is also given just to explain the development of building materials in time. In the second chapter, the composite material is discussed from all perspectives – its composition, structure and properties of its constituents and fabrication of the composite. A literature review on experiments concerning the durability of bond after freeze/thaw cycles is also presented. In the next chapter dealing with numerical approach, mechanical properties of the composite material are calculated using different methods. Then modeling of heat transport in MATLAB is then presented and confronted with an independent software. In the third part of this chapter a model of the concrete beam in ATENA software is used to estimate the load-bearing capacity of experimental beams. The fourth chapter containing experimental approach describes how the specimens were fabricated, prestressed, cured, loaded with temperature in a climatic chamber and subjected to a four-point bending test. Discussion and results are presented in the same chapter. In the last chapter, conclusions are deduced and further research is outlined.

Chapter 2

State of the art

A composite material – as the name suggests, is a heterogenous material made of two or more physically and chemically different components (or phases) in order to make a new material. Due to synergic concurrence of individual constituents this material has enhanced properties compared to the sum of its constituents.

Generally it is possible to divide composite materials according to the geometry of the reinforcing factor [5]. They can be fibrous or particle composites. Particle composites can be either orientated or non-oriented. Fibre concrete makes a nice example of a non-oriented particle composite on mesoscale. Fibrous composites are either one or multilayered. Multilayered can be sandwiches or laminates (multilayered yarns, chopped strand mats or braids soaked with a matrix). One-layered composites consist of strands of fibres covered in a matrix.

2.1 Structure of FRP

The main components are *reinforcement* (usually fibres, but also particles or flakes) covered with a polymer *matrix*. Additional components may also be added in order to modify the properties of the composite. These can be *fillers* and/or *additives*.

Fibres are embedded in the matrix and serve as a reinforcement. They provide crucial mechanical properties of the composite such as strength and stiffness and determine the properties of the composite in the longitudinal direction. Fibres also serve as the main load-bearing element of the composite. The size of individual fibres (or filaments) is 5 – 20 μm . The smaller the diameter of the fibre, the stronger it is, because the structure of the fibre can contain less imperfections (i.e. voids and pores). Too small fibres can be dangerous however, because inhaling them they could cause cancer [6]. The larger the diameter of the fibre, the more resistant the composite is to buckling in compression. Thousands of individual filaments are bundled together to

form tows, strands, rovings or braids. Carbon tows are marked according to the number of filaments they contain, i.e. 3k (=3000), 6k, 12k etc. . . . Rovings or braids can be woven or stitched together under different angles and patterns to form fabrics.

Matrix provides bond between individual fibres and distributes strain among them. It covers and protects them from damage during production of the composite and through the service life of the product. It also determines the electrical and chemical properties of the composite. The material for matrix can be a polymer, metal or ceramic. [7]

Fillers can improve mechanical properties of the matrix if necessary. Usually hollow micro-balloons of glass, carbon or organic material are added into the polymer in order to lower the density, improve workability or mechanical properties (such as strength or toughness). Fillers can be added also to decrease the price of the matrix, improve fire resistance or electrical conductivity, whatever is needed for the planned application of the composite.

Additives are added into the polymer to improve its durability under UV light, decrease shrinkage or simply change the colour of the polymer.

The resultant properties of the *FRP* (Fibre Reinforced Polymer) depend on the mechanical properties of its constituents, the ratio of fibre to resin (described by the fibre or resin volume fraction – FVF or RVF respectively), the orientation of reinforcing fibres and on the interphase between fibres and matrix. The problem is that when the material is manufactured, its structure is always different (when considering two products - even when on macroscale they may look the same, their microstructure is different). The method of fabrication and type of reinforcement determine the FVF so every property is linked. When designing structures the designer has to consider the material used as a whole, starting from the manufacturing to the final product with specific properties. As V. Pompe [8] pointed out:

“The application of composites as a bare replacement instead of metals doesn’t allow to fully exploit its potential and can be counter-productive. In order for a structure to be maximally effective, it has to be designed as a composite structure from the beginning and even considering the manufacturing of the composite”

The design of composite structures is a complex procedure. The designer has to take into consideration that composites are no more isotropic materials (such as steel) but usually orthotropic or (depending on the product) transversally isotropic. Their

properties depend on the structure of the material and the orientation of reinforcing fibres – in one direction the final product can be six times stronger than steel while in the perpendicular direction soft as polymers.

When comparing composite materials with steel several things have to be taken into account. First let us consider the *elastic modulus to nominal strength* ratio. By comparing these ratios for both materials we see that composites actually do not exceed steel. But when one takes into account weight and compares *nominal density to strength* ratio then composites generally surpass steel. This shows that a structure can be designed much stronger using composite materials if the shape of the product is given or it can be much lighter with the same load-bearing capacities as the same products made from steel.

Two most important components of the composite, i. e. fibres and matrix, are discussed in greater detail in the following chapters.

2.2 Fibres

Mentioned below are the most frequently used reinforcing fibres in FRP for *civil engineering* purposes:

- *glass* – GFRP (Glass Fibre Reinforced Polymer)
- *carbon* – CFRP (Carbon Fibre Reinforced Polymer)
- *aramid* – AFRP (Aramid Fibre Reinforced Polymer)

Other types of fibres are also used, mainly in *mechanical engineering*:

- *basalt*
- *quartz*
- *boron*
- *ceramic* (SiC, Al₂O₃)
- *metal* (stainless steel, tungsten, molybdenum)

At the end of this chapter a comparison of mechanical properties for the most frequently used fibres is shown in Figure 2.4.

2.2.1 Glass fibres

This amorphous inorganic material consists of silica oxide SiO_2 (more than 50 %), calcium oxide CaO , aluminium oxide Al_2O_3 and various other oxides. Based on its chemical structure this material is isotropic. It is also relatively lightweight, inexpensive and easy to manufacture. These properties allowed it to be widely used in industrial applications.

- **Fabrication** [6, 7] – glass fibres are produced by melting raw materials (silica sand SiO_2 , boric acid $\text{B}(\text{OH})_3$, limestone CaCO_3 , china clay $\text{Al}_4[\text{Si}_4\text{O}_{10}](\text{OH})_8$, dolomite $\text{CaMg}(\text{CO}_3)_2$ and fluor spar CaF_2) in a refractory furnace. The melting temperature varies around 1540°C in the furnace and 1425°C in the homogenization sector. The melt is then transported to a forehearth where a series of platinum bushings (1-2 mm wide) forms individual filaments. These filaments are then pulled mechanically to reduce their diameter. The pulling speed is up to 50 m/s. The faster the pulling speed, the thinner the diameter of filaments.

These filaments are extremely fragile and manipulation causes abrasion on their surface, resulting in decreased mechanical properties. To reduce the abrasion and surface damage and on the other hand to improve wetting by the matrix, a chemical sizing (i.e. organic coating) is applied on the surface of the filaments coming out of the bushings. Sizing can be temporary so another chemical finish (typically polyvinyl acetate modified with chromic chloride complex and/or organosilane coupling agents) is sprayed on the fibres to improve adhesion between the organic matrix and anorganic fibres. The interface between them is a weak spot for this composite because a chemical attack or humidity can cause corrosion and deterioration of bond.

- **Properties** [9] – glass fibres are widely used because of their low price and good mechanical properties. Ultimate strength of a single fibre was measured up to $f_u = 3500$ GPa. But this was for an undamaged fibre right after manufacturing. Further processing of glass fibres and residual stresses from shrinkage reduce their strength up to 50 %. The elastic modulus is similar to aluminium, i. e. around 75 GPa (depending on specific type of glass). Glass fibres have a linearly elastic behaviour, elastic strain is around 4 %. Fibres are non-flammable, but their mechanical properties deteriorate as the temperature increases. Moisture can have a serious impact on glass fibres because it enables acids or alkalis to reach the surface of the fibre. These then damage the surface and fasten the propagation of microcracks that glass fibres have after processing. As long as the matrix remains uncracked it protects the inner fibres in the composite but the outer fibres are vulnerable to this hazard.

There are many types of glass fibres varying slightly in chemical structure (see Table 2.1), but greatly in performance and mechanical properties (see Table 2.2 and Figure 2.1).

- *E-glass* – the most frequently used because of its lowest production price. It is dominantly composed of silicon, calcium, aluminium and boric oxide (SiO_2 , CaO , Al_2O_3 , B_2O_3 , respectively). It has a good combination of mechanical properties, chemical, electrical and corrosion resistance. At elevated temperatures the molecules rearrange into a less compact shape, making the product more flexible. E-glass is, however, non-flammable.
- *R-glass* – a high performance glass, in Europe called R-glass, S-glass in America and T-glass in Japan. These are simply different names for the same chemical structure of glass. It contains only silicon oxide SiO_2 , aluminium oxide Al_2O_3 , magnesium oxide MgO and a minimum of other oxides. It has a much higher strength (by approx. 40 %) and stiffness than E-glass. However it is used only for high-end applications where high strength can compensate its high cost. But the price is so high that designers have to decide if the value-performance ratio is sufficient to justify the cost for the application. And if not, with only a slight increase in price carbon fibres are available.
- *C-glass* – has a modified chemical structure containing more oxides than S-glass. The specific mixture provides corrosion resistance due to acids and chemically aggressive substances [6]. With a slight modification (exclusion of boric oxide B_2O_3) a so called *ECR-glass* is created. This glass is very stiff with superior resistance to acids.
- *AR-glass* – again by modifying the chemical structure of the basic E-glass by adding zirconium oxide ZrO_2 [10], alkali-resistant glass can be fabricated. These have a high resistance to alkali attack making them useful in reinforcing concrete structures.

2.2.2 Carbon fibres

This material is composed of randomly layered sheets of hexagonal rings of carbon atoms [7]. Mechanical properties depend on the orientation of carbon chains making this material strongly anisotropic. These fibres have supreme mechanical properties (highest specific strength and modulus) compared to glass or aramid fibres. They are mostly used in high-end applications in aerospace industry.

Table 2.1: Chemical composition of glasses in weight % [6, 7]

		E-glass [%]	R-glass [%]	C-glass [%]	AR-glass [%]
silicon oxide	SiO ₂	52–56	65	64–68	62
aluminium oxide	Al ₂ O ₃	12–16	25	3–5	–
calcium oxide	CaO	16–25	–	11–15	5–9
boric oxide	B ₂ O ₃	5–10	–	4–6	<0,5
magnesium oxide	MgO	0–5	10	2–4	1–4
zirconium oxide	ZrO ₂	–	–	–	17
additional oxides	–	–	–	–	–

Table 2.2: Typical properties of glass fibres [6, 9, 11]

	Tensile strength [MPa]	Elastic modulus [GPa]	Ultimate tensile strain [%]	Density [kg/m ³]	Poisson's ratio [-]	Longitudinal thermal expansion ·10 ⁻⁶ [K ⁻¹]
E-glass	3 450	72	4,8	2 500	0,22	5,04–5,4
R-glass	4 800	85	5,6	2 480	0,22	1,6–2,9
C-glass	3 310	69	4,8	2 560	0,22	3,3–4
AR-glass	3 700	77	4,8	2 680	n/a	6,5

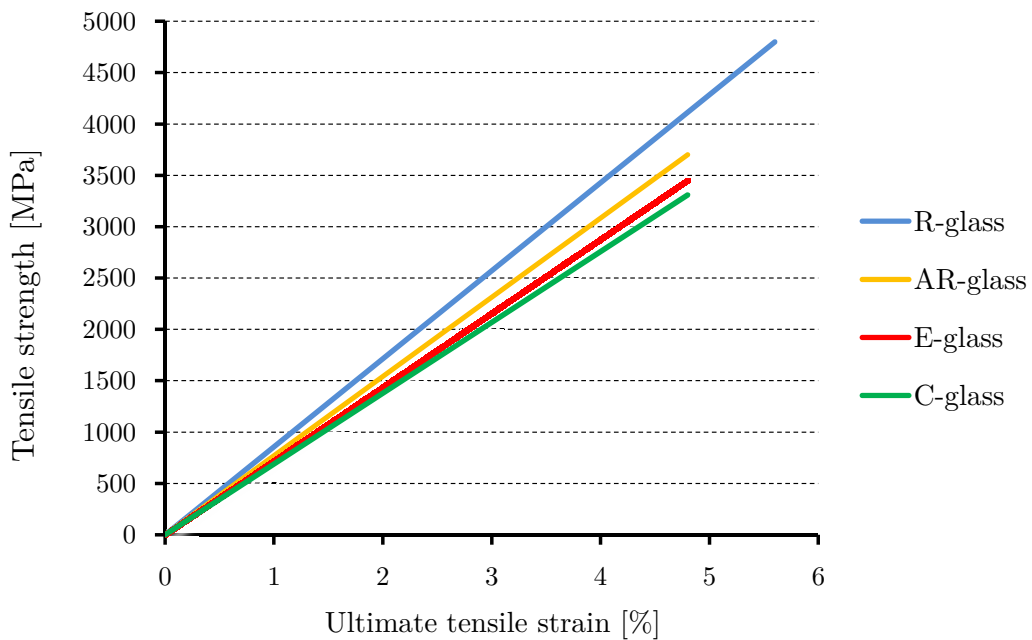


Figure 2.1: Stress–strain diagram for glass fibres [9, 11]

- **Fabrication** – carbon fibres can be produced from three different raw materials, or *precursors*: cellulose, pitch or polyacrylonitrile (PAN). Depending on which

precursor is used the final mechanical properties are determined. Cellulose-based fibres are used for insulation against high temperatures, pitch-based fibres have a high elastic modulus while PAN fibres have high strength. PAN fibres are widely used and serve as an industry standard. The fabrication process is similar for all precursors.

During the first fabricating process the fibres are stretched. This orientates the graphite crystals (that will form later on) to obtain better mechanical properties by stabilizing the inherent shrinkage of the PAN fibres. Fibres are then heated to 200-300 °C. In the next step fibres are pyrolyzed in an inert atmosphere of nitrogen or argon between 1000-1500 °C [12]. This step is called *carbonization*. Temperature is further increased up to 2000-3000 °C in the last stage called *graphitization*. Nitrogen atoms are removed and sheets of hexagonal carbon atoms are layered at each other producing a crystalline structure [7].

After the heating process is completed the surface of the fibres is treated by sizing. There are two types of this treatment: oxidative and non-oxidative. Both processes improve wetting by the matrix but through different means. During oxidative treatment the fibres are drawn through a nitric acid bath or alkaline electrolytic bath. During this process hydroxides are attached to the surface of the fibre providing better bond with the matrix. Non oxidative treatment can be done in three ways: whiskerization (single crystals of ceramic materials are grown on the surface perpendicular to the orientation of the fibre), pyrolytic coating (pyrolytic carbon in vapor phase is deposited on the surface) or polymer grafting (similar to oxidation) [7].

Two different types of fibre are produced: *carbon* fibres and *graphite* fibres. Carbon fibres are produced around 1300 °C and contain approximately 93-95 % carbon and 5-7 % nitrogen. Graphite fibres contain approximately 99 % carbon atoms but a much higher temperature (cca. 2400 °C) is needed to purify the structure of the fibre.

- **Properties** – carbon fibres can be generally separated into two groups. The first is produced from graphite fibres, has a high elastic modulus (reaching up to 500 GPa) but lower strength (a.k.a. *high modulus*). The other group made from carbon fibres has high strength (up to 3500 MPa) but lower modulus (a.k.a. *high strength*).

Generally carbon fibres have a linear elastic behavior. These fibres are very brittle because their elongation is very limited (only around 1 %). But their supreme corrosion and fatigue resistance, vibration damping and very light weight ($< 2000 \text{ kg/m}^3$) makes them useful in demanding applications (such as aerospace industry). Their anisotropy strongly influences their mechanical properties such as coefficient of thermal expansion – in the longitudinal direction it is negative while in the perpendicular direction it is positive (see Table 2.3 and Figure 2.2). They also conduct electricity very well. Thermal stability of properties within temperatures up to $2000 \text{ }^\circ\text{C}$ makes them very useful in engineering applications. And the only drawback is the price of this material. Being roughly 10 times more expensive than glass fibres and almost a 100 times more expensive than normal steel makes this material with great properties applicable only in some areas, where its high price can be justified. The high cost of these fibres is caused by the high price of raw materials and the long process of carbonization and graphitization [10].

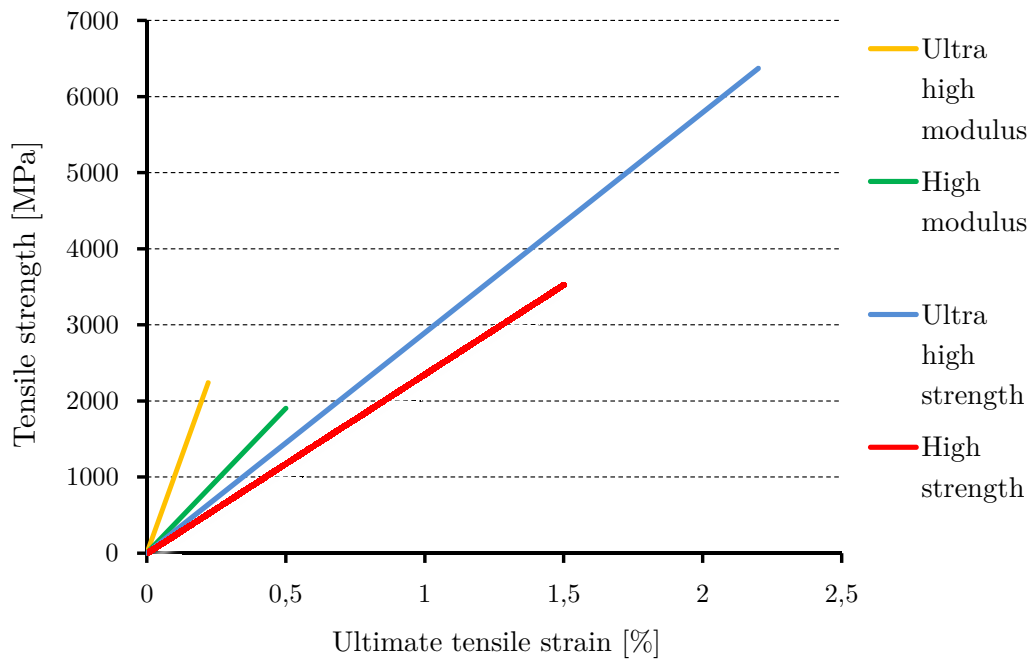


Figure 2.2: Stress–strain diagram for carbon fibres [9, 13, 14]

2.2.3 Aramid fibres

Aramid fibre is an organic fibre made from a polymer compound. It consists of carbon, hydrogen, oxygen and nitrogen [12]. Similar to carbon fibre it is strongly anisotropic due to its chemical structure, even having a negative longitudinal CTE.

These fibres are very attractive because of their very low weight. Due to this the specific strength (i. e. strength-to-weight) and stiffness (stiffness to weight) ratios are the highest among reinforcing fibres (see Table 2.3). They can absorb large amounts of energy from impacts which is used for fabrication of bulletproof vests. Other applications include a rubber reinforcement in tyres, high strength fabrics and everywhere, where high strength and low weight are essential.

- **Fabrication** – the manufacture starts with dissolving of a solid polyamide (highly crystalline fibres with strongly oriented molecules) in an organic solvent such as a strongly concentrated sulfuric acid. After polymerization the polymer has partially orientated molecules. It is then extruded into hot cylinders at 200 °C and washed. To increase its stiffness and strength it is stretched after cooling [6, 7, 12].

Aramids generally show out poor bonding with a matrix. This can be an advantage though because it improves the absorption of energy from impacts.

There are many organic fibres produced but the best known is *aramid*. Trade names include *Kevlar*, *Technora* or *Twaron* (among others) that are manufactured by DuPont, Teijin and AkzoNobel respectively. Kevlar is made in three types (with increasing modulus due to the additional crystallinity produced in the manufacturing process): *Kevlar 29* (used for bullet-proof vests), *49* (widely used for a broad range of applications) and *149* (best mechanical properties but at a price).

- **Properties** – aramid fibres are the lightest fibres produced having a nominal density around 1,45 kg/m³. Aramid molecules are very strong because of rigid aromatic rings orientated in the direction of the fibre but weak in the perpendicular direction. This is because of weak hydrogen bonds resulting in anisotropic properties of the fibre. Fibres are best used in structures subjected to tensile stresses but not compressive stresses or bending. The stress-strain diagram is linear with a higher ductility than carbon fibres (around 2-4 %).

These fibres have a few disadvantages on the other side. They have a low compressive strength (see Figure 2.3) but a very high ductility in compression making it extremely useful in absorbing energy from impacts. As other organic fibres their properties decrease with increasing temperature. They are sensitive to UV light which also damages these fibres. Fibres creep and also are hydrophilic (absorb

water) which deteriorates bond with the matrix (thus fibres have to be dried and coated prior to wetting by the matrix).

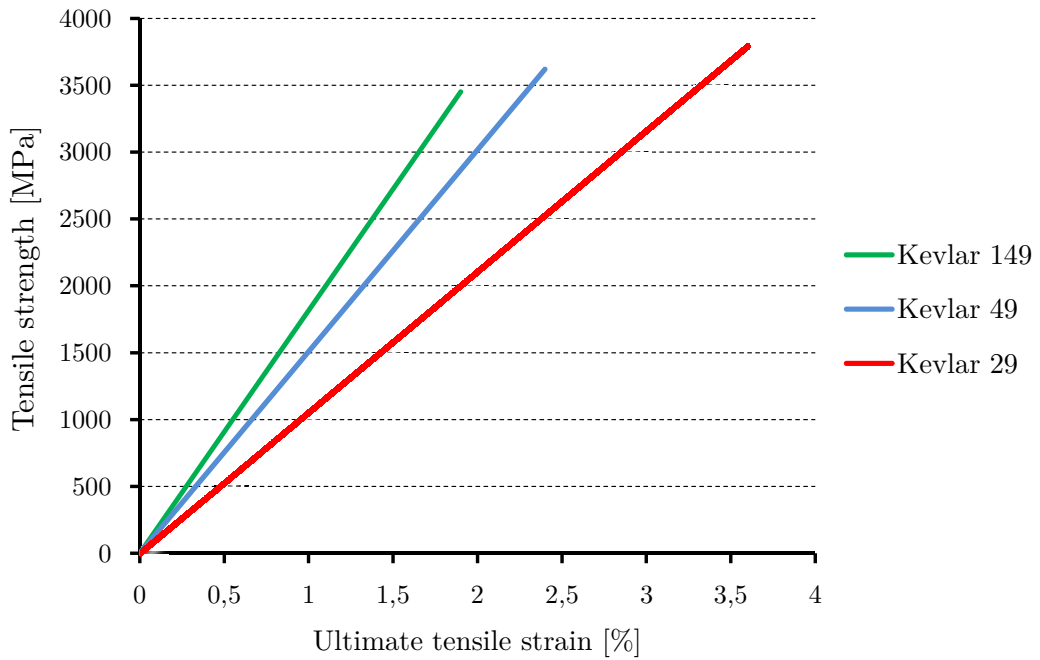


Figure 2.3: Stress-strain diagram for aramid fibres [9, 15]

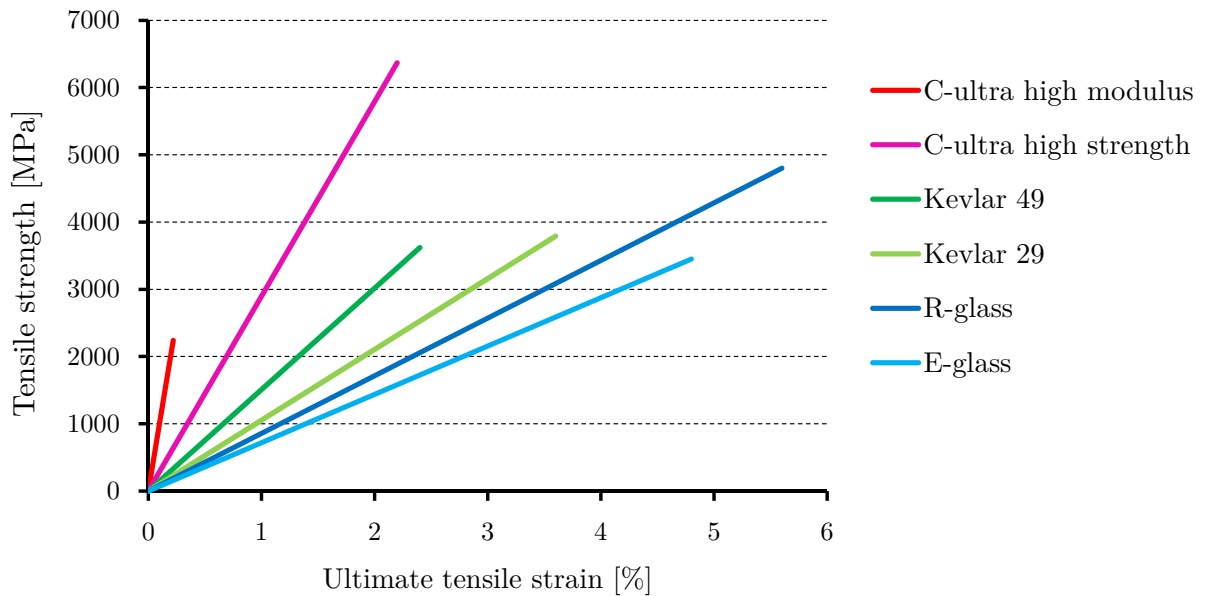


Figure 2.4: Comparison of stress-strain diagrams for the most frequently used fibres

Table 2.3: Typical properties of carbon and aramid fibres [9, 10, 13, 14, 15]

Type	Tensile strength	Elastic modulus	Ultimate tensile strain	Density	Poisson's ratio	Longitudinal thermal expansion	Transversal thermal expansion
	[MPa]	[GPa]	[%]	[kg/m ³]	[-]	$\cdot 10^{-6}$ [K ⁻¹]	$\cdot 10^{-6}$ [K ⁻¹]
Torayca T300 (PAN)	3 530	230	1,5	1 760	0,2	-0,41	7-12
Torayca T1000 (PAN)	6 370	294	2,2	1 800	0,2	-0,55	-
Thornel P55 (pitch)	1 900	380	0,5	2 000	0,2	-1,3	-
Thornel P100 (pitch)	2 240	830	0,22	2 130	0,2	-1,6	-
Kevlar 29	3 792	75	3,6	1 440	0,35	-2,2	59
Kevlar 49	3 620	131	2,4	1 450	0,35	-2,7	59
Kevlar 149	3 450	179	1,9	1 470	0,35	-	59

2.3 Matrix

A matrix is a component that covers and binds together individual fibres, protects them from damage during production (prevents damage by reducing mechanical abrasion between individual fibres), manipulation and during service life of the composite material from environmental hazards. It holds individual fibres in place, provides bond and distributes strain evenly among them. The material of matrix determines conditions under which the composite material can function. These include thermal and chemical resistance, electrical conductivity or durability. While strength and stiffness of the composite are governed mainly by fibres, several important mechanical properties depend mostly on the matrix such as transverse stiffness and strength, shear modulus and strength, thermal expansion and resistance and fatigue.

According to the material used for a matrix, mentioned below are the most frequently used matrixes for *civil* and *mechanical engineering* purposes [5]:

- *polymer* – (PMC – Polymer matrix composite), discussed in greater detail below
- *metal* – (MMC), Al, Ti, Mg, Ni alloys
- *ceramic* – (CMC) Al_2O_3 , Si_3N_4 , SiC, highly resistant to temperature
- *carbon* – carbon-carbon composites, bio-compatible
- *glass* – high temperature applications

A polymer is called a *resin system* during polymer processing and *matrix* after processing [10]. A polymeric matrix can be separated into two groups – *thermoset* and *thermoplastic* resins. These will be discussed in the following chapters.

2.3.1 Thermosetting resins

Chains of many small molecules in the resin are heavily cross-linked, forming strong covalent bonds during curing. This creates an indissoluble and infusible rigid molecular structure that has a low coefficient of thermal expansion and less flow (under stress) [10]. The lower the viscosity of the resin, the better and easier the wetting of fibres can be achieved. These resins retain their shape after curing and do not melt when exposed to high temperatures. Until *glass transition temperature* is reached, they provide high thermal insulation. A negative effect caused by the change of volume occurs during curing – volumetric shrinkage. This causes internal stress, microcracking of the fibres and uneven surface of the composite. It varies from 4 % for epoxy to 8 % for polyester.

There are three main types of thermosetting resins used in civil engineering applications:

- *polyester* – are low viscosity, clear liquids based on unsaturated polyesters which are dissolved in a reactive monomer (for example styrene). Heating and adding organic peroxide (a free radical initiator) starts a cross-linking reaction (carbon-carbon double bond) between polyester and monomer and forming a 3D structure [10]. Great volumetric shrinkage (around 8 %) occurs during this exothermic reaction.

These resins offer high value for a low cost, great variability of properties by modifying their chemical structure, making them widely used. They have low viscosity (depending on the amount of styrene) which helps wetting of the fibres. They are used when corrosion resistance (in strong acid environments) is needed or when stability under UV light is required.

- *vinyl ester* – differ from polyesters in their chemical structure containing less cross-linked molecules. The bridging is performed by methacrylate. This makes higher elongation possible. They are frequently used for GFRP because of their higher corrosion resistance (to acids, alkalis or solvents) and higher stability at elevated temperatures than polyester.
- *epoxy* – are low molecular weight organic liquids that are characterized by epoxy groups – rings containing two carbon and one oxygen. To initiate polymerization (cross-linking of molecules), reactive curing agents are added into the liquid. The more cross-linked molecules, the better mechanical and thermal properties of the resin after curing. Adding thermoplastics such as hardeners (to aid curing), plasticizers (improve toughness, flexibility and ductility) and fillers (to lower the cost and increase strength or UV resistance) [12] can further improve the properties, at a price.

Their properties are proportional to their price: 3–4 times higher than polyester resins. They have the highest mechanical properties (compared to other thermosetting resins), highest chemical resistance, simple curing (from 5 to 150 °C) and provide excellent electrical insulation. Due to low viscosity their shrinkage during curing is very low (approx. 1,5 – 4 % by volume), providing excellent bond to other materials (fibres for example). The disadvantage is their price and long curing periods (hours up to days).

Table 2.4: Typical properties of thermosetting matrixes [5, 9]

	Tensile strength [MPa]	Elastic modulus [GPa]	Ultimate tensile strain [%]	Density [kg/m ³]	Poisson's ratio [-]	Coefficient of thermal expansion ·10 ⁻⁶ [K ⁻¹]
Polyester (isophthalic)	75,9	3,4	3,3	–	0,38	30
Vinyl ester (Derakane 411)	82,7	3,4	5,5	–	0,38	–
Epoxy (8552)	100	4,67	4,4	1272	0,38	54

2.3.2 Thermoplastic resins

Thermoplastics are solid materials under normal temperatures. They have to be heated over their melting temperature (more than 200 °C) in order to break weak bonds (van der Waals type) between long chains of molecules. During processing the resin softens but their chemical structure remains unchanged. Perfect impregnation of fibres is hampered by the high viscosity of these resins. However, the hardened matrix can be repaired if needed by melting the resin without significant degrading, making this material recyclable. These resins can be used to make stirrups and other shear reinforcement. But high viscosity (compared to thermosets) increases the price of this resin due to the demands for a high temperature and pressure during processing.

Typical examples of thermoplastics include the traditional polyethylene (PE), polyvinylchloride (PVC) and polystyrene (PS). But today high performance thermoplastic resins were developed, for example polyether-ether-ketone (PEEK), polysulfone (PSUL) or polyetherimide (PEI). An overview of their mechanical properties can be found in Table 2.5.

Table 2.5: Typical properties of thermoplastic matrixes [9]

	Tensile strength [MPa]	Elastic modulus [GPa]	Ultimate tensile strain [%]	Density [kg/m ³]	Poisson's ratio [-]	Coefficient of thermal expansion ·10 ⁻⁶ [K ⁻¹]
PEEK	100	3,24	50	1320	0,4	47
PSUL	70,3	2,48	75	1240	0,37	56
PEI	105	3	60	1270	0,37	56

2.4 Fabrication process

Many techniques were developed to manufacture composite materials. The choice of the process is determined by the properties of the constituents, FVF, thickness of the composite and the cost effectiveness of the final product. The most frequently used fabrication techniques include hand or prepreg lay-up, bag moulding, autoclave processing, compression and resin transfer moulding, filament winding and pultrusion.

The highest volumes of fibres can be achieved with filament winding or pultrusion processes (up to 65 % and 83 % respectively [5]). What may seem as a weakness when comparing composites to isotropic materials is that the structure of the composite is slightly different, as the composite is formed each time as new. The properties of the final product are always slightly different. The typical manufacturing process to create FRP rebars is pultrusion and it will be discussed in greater detail.

Pultrusion was invented in the 1950s by W. B. Goldsworthy [2]. It is a relatively fast continuous process (see Figure 2.5) used to fabricate low cost, constant cross-section elements of any length such as rods, beams, panels or plates. It is used for applications where high volume of production predominates over the quality of the final product. Operational costs are kept at a minimum as low cost fibres (dominantly E-glass) and thermosetting resins (usually polyester because of its low viscosity or vinyl ester if better corrosion resistance is required) are used. The drawback is that the pultrusion line requires enough space because of the necessary length of the curing sections.

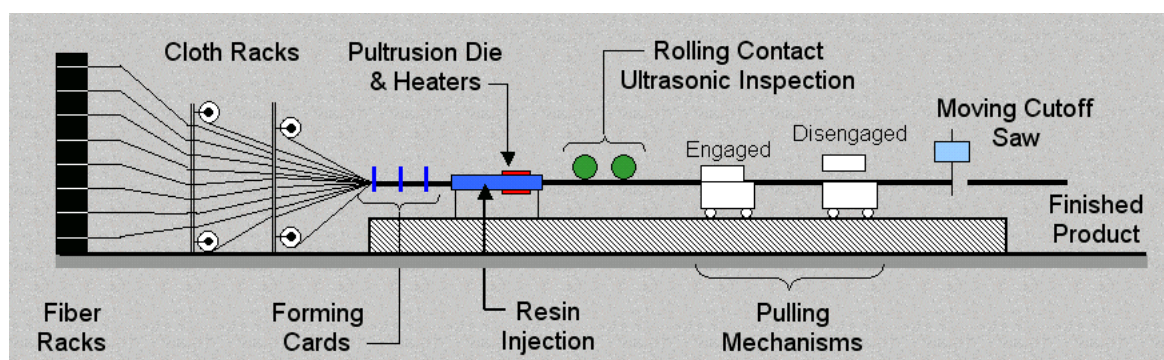


Figure 2.5: Scheme of a pultrusion line [16]

Fibres are pulled from mat racks and guided to forming cards. During this process fibres can be preheated (using radio frequency heaters) when thick parts are made (up to 12 mm) or thermoplastic resin is used [9]. Fibres then continue into the die where they are injected under pressure with resin (containing catalysts, fillers and pigments) and processed further. Wet fibres are then shaped in the needed cross-section, heated

and cured. The cured part is pulled further and the product is cut by a diamond tipped saw to the required length.

Slight modifications to this process can be made depending on the product produced. To reduce damage to glass fibres during pulling from fibre racks, the fibres can be pre-wetted by a resin. When FRP rebars for reinforcing concrete are produced, the die is not heated. Instead, curing is accomplished in tunnel-oven. Wet fibres are guided through a sizing brush which removes entrapped air and excess resin [9]. Fibres are then formed into the desired cross-section in the die, wrapped with a roving (flaxen cord) and covered with glued sand. Then the final product is cured in a tunnel oven.

2.5 Features of FRP composites

The properties of composite materials depend on many factors, among others the properties of fibres and resin, their volume fraction and orientation or manufacturing method. And as every other building material it has certain properties (mentioned below) that have to be taken into consideration when reinforcing structures using FRP. They can substitute ordinary steel reinforcement but not in every aspect and with different outcomes.

Advantages

- *specific strength and stiffness* – in composites determined by *tenacity* – strength to weight ratio. Glass fibre composite (GFRP) rebars reach strengths from 450 up to 900 MPa with a densities of 1600 – 2000 kg/m³, giving us specific strength of 0,45 MPa m³/kg. Carbon fibre composites (CFRP) have strength up to 3000 MPa and density up to 2100 kg/m³, giving tenacity of 1,43 MPa m³/kg. When comparing them to steel reinforcement (500 MPa, 7850 kg/m³, 0,06 MPa m³/kg), composite materials can be more than 20 times stronger. When considering only the strength of rebars alone, GFRP are 1,3 times stronger than steel, while CFRP up to 6 times.
- *durability* – is determined by the matrix and generally is one of the main advantages over steel reinforcement. GFRP does not corrode (at least not in the same way as steel) and is resistant to environmental and chemical attacks (in alkaline environment like concrete). FRP reinforcement is best used in aggressive environment (such as marine or coastal structures, industrial powerplants, extremely thin structures or simply in foundations of buildings).
- *weight* – as mentioned in the specific strength section, FRP is much lighter than steel. Weight depends on the fibres and matrix used (and their volume fraction)

but it can generally be stated that typical weight for FRP varies from 1250 – 2300 kg/m³. Thanks to its corrosion resistance the concrete cover can be also reduced and dimensional (cross-sections) and weight savings can be obtained on structures. The use of lightweight reinforcement can speed up construction. FRP is also used as a external bonding reinforcement and its light weight does not present additional load for the structure.

- *electromagnetic neutrality* – FRP does not interfere with electro-magnetic fields so it can be used for hospitals where MRI (magnetic resonance imaging) takes place or for magnetic railway systems.
- *non-conductibility* – is not valid for CFRP but other reinforcements can be used on railway bridges, where stray currents cause corrosion of internal reinforcement and stainless steel is too expensive.
- *fatigue resistance* – while not exactly a civil engineering prerequisite, FRP show greater resistance to fatigue than metals.

Disadvantages

- *non-isotropic behavior* – even though glass fibres are isotropic, carbon and aramid are strongly anisotropic. The final composite behaves as a transversally isotropic material. The mechanical properties depend on fibres and their orientation in the final product. The properties perpendicular to the orientation of fibres are ruled by the matrix and these are usually much lower. Even more material constants of constituents are necessary to estimate the mechanical properties of the composite.
- *flexibility* – FRP have a very low elastic modulus. It depends mainly on the fibres but as it can be seen from Tables 2.2 and 2.3, the resultant values for FRP vary from 20 – 50 GPa for glass, 60 – 120 GPa for aramid and 100 – 150 GPa for carbon. Elastic strain capacities of FRP range from 1,5 – 2 % but other building materials such as steel (0,2 %) or concrete (0,35 % of cracking strain under compression [2]) are dramatically different. This brings additional problems for designing structures reinforced with FRP. Design guidelines are not available (up to date) and when codes for RC are used the calculations are inaccurate.
- *brittleness* – FRP composites retain the linear elastic behavior of the reinforcing fibres. But since ductility is requested from reinforcing members, experiments by D. Choi [17] concerning mixing fibres in different ratios in one composite are taking place in Japan. By combining glass and carbon fibres in a ratio approx. 8:1 some pseudo-ductility can be observed.

- *lack of bending* – depends on the type of matrix used since thermoplastic matrixes can be manipulated upon heating. But due to the high price for the thermoplastic matrix usually thermosetting matrixes are used for FRP reinforcement. Lack of bending and brittleness of the hardened matrix can cause microcracks in the matrix which can propagate and damage fibres. Enhanced cautiousness is therefore necessary when manipulating the reinforcement on building site.
- *cost* – when adding together the cost of raw materials and the fabrication cost, the overall price is extremely high when compared to ordinary steel. This material comes out very uneconomical when only initial costs are considered. But LCC should be taken into account. Steel-reinforced structures usually need repairs because of corrosion problems after only 30 years of service (i. e. one third of their designed life span). These additional costs increase the overall cost of building.
- *combustibility* [2] – the weakest link in FRP is the polymer matrix. Regardless of specific chemical composition of the polymer, upon reaching the glass transition temperature a dramatic decrease of polymer's mechanical properties occurs. As the temperature increases the polymer softens, melts and ignites at cca 250 °C. The matrix stops providing bond between fibres and as the result the rebar loses its stiffness and capacity to transfer load. Glass transition temperature is unique for each polymer and depends on its chemical structure. A. Sumida tested the resistance of various FRP rebars to fire and measured that regardless of specimens used 100 °C was critical for most FRP [18]. Concrete protects the internal reinforcement from fire. But due to the low elastic modulus of FRP big deflections occur on structures. This causes excessive crack propagation exposing the FRP to outside environment. The load bearing capacity of the structure is not challenged but through cracks, fire can reach the FRP rebars causing an increase in temperature and probably the combustion of the matrix.

2.6 Mechanical properties of FRP

One of the great benefits of composites is the *synergical effect* on the material's behaviour. Because of it the resultant properties of the composite are better than the elementary sum of properties of individual constituents.

Composites generally display anisotropic behaviour similar to wood for example. The mechanical properties depend on the orientation of the reinforcing fibres and matrix. In case of composite bars the fibres are mostly orientated in the longitudinal direction. Therefore we can point out two directions of anisotropy: in the direction of the fibres (axis 1) and perpendicular to them (axis 2 and 3). The direction perpendi-

cular to the orientation of fibres forms a plane of symmetry for the properties. This configuration is called *transversally isotropic material*. Only 5 independent material constants E_1 , E_2 , G_1 , G_2 and ν_{12} have to be investigated in order to get the resultant properties (see Section 3.1 in Chapter 3).

The *mechanical behaviour* of FRP composites is linear elastic until a brittle failure occurs, as seen on Figure 2.6. The elastic capacity of the composite is governed by the maximum allowable strain in the fibres, generally around 5 % for glass fibres, 2 % for carbon fibres and 2,5 % for aramid fibres. There is no detectable yielding, plastic deformation or hardening when comparing FRP to steel reinforcement (see Figure 2.7). The low elastic modulus of FRP causes excessive crack propagation on structures but this effect can be diminished by prestressing the rebars.

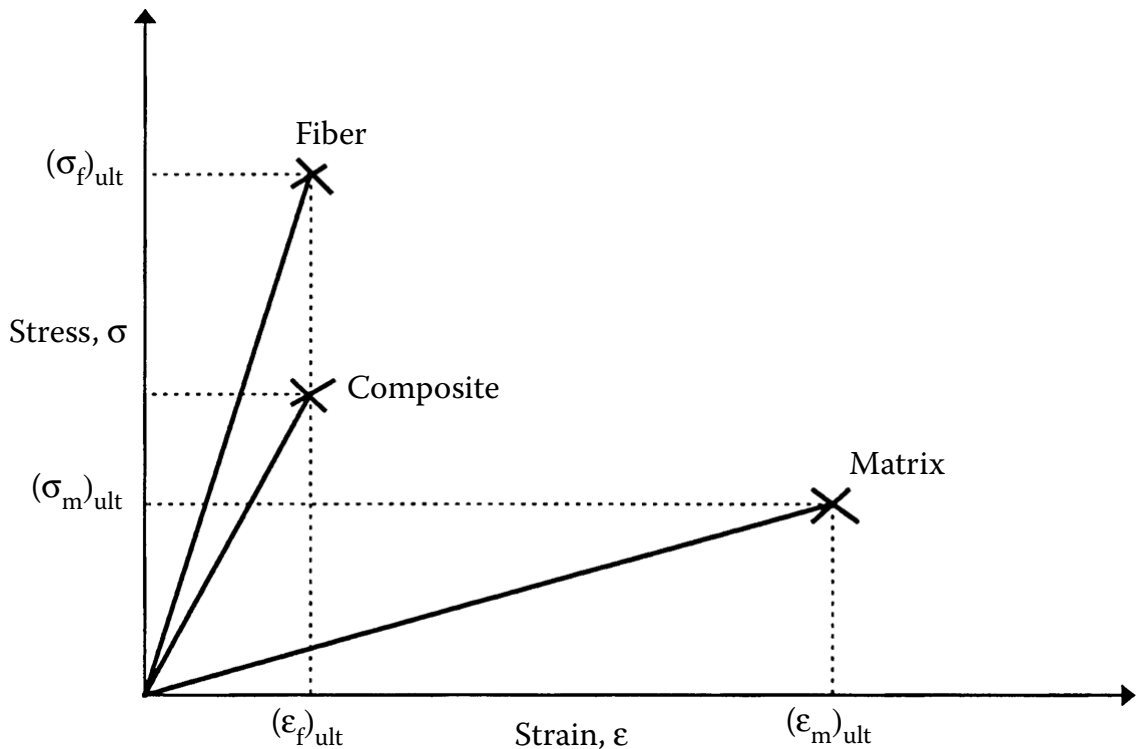


Figure 2.6: Stress-strain diagram for FRP [12]

Typical properties of FRP composites depend on a number of factors, mainly on the fibres and matrix used, their ratio (defined by FVF) but a general overview is presented in Table 2.6.

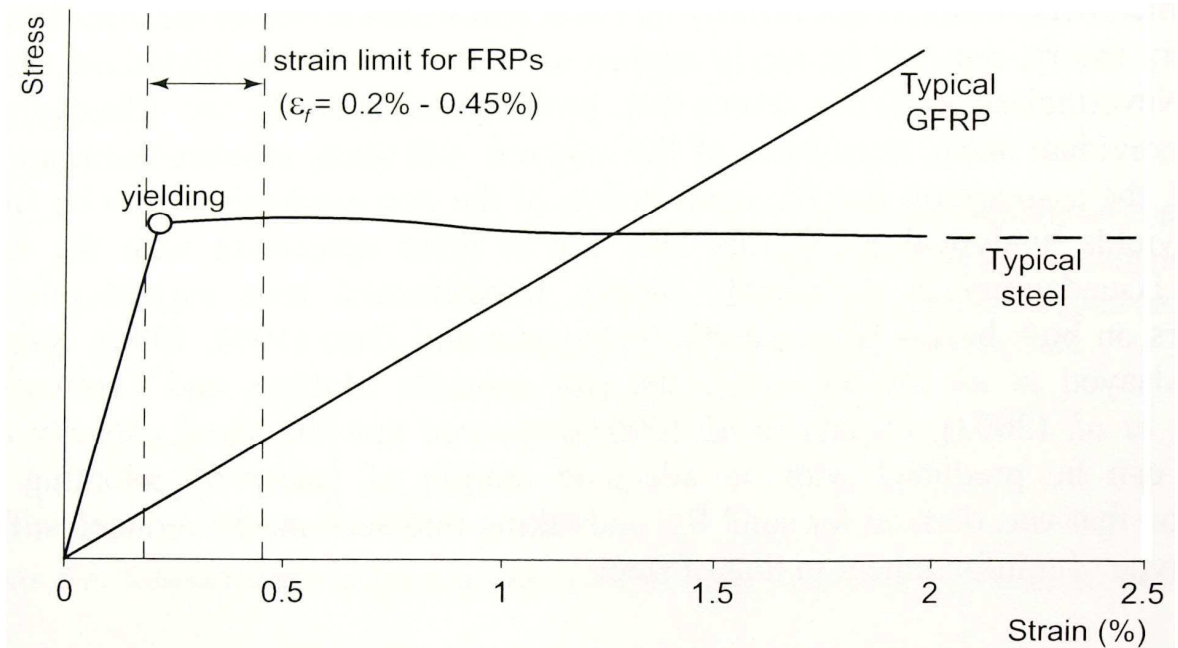


Figure 2.7: Comparison of stress-strain diagrams for steel and GFRP [10]

Table 2.6: Typical properties of FRP, steel and concrete [2, 10]

	Tensile strength [MPa]	Elastic modulus [GPa]	Weight [kg/m ³]	CTE <i>longitudinal</i> ·10 ⁻⁶ [K ⁻¹]	CTE <i>transversal</i> ·10 ⁻⁶ [K ⁻¹]
GFRP	450–1 600	35–60	1 700–2 100	6–10	25–50
CFRP	600–3 500	110–580	1 400–1 700	-9–0	74–104
AFRP	1 100–2 500	65–120	1 250–1 450	-6 – -2	60–80
Steel	400–600	210	7 850	11,7	11,7
Concrete	12–90	27–44	2 300	7–12	7–12

Note: Compressive strength for concrete

2.7 Thermal properties of FRP

Thermal properties become increasingly important when considering FRP reinforcement in concrete. Concrete is an isotropic material and its CTE is around $7 - 12 \cdot 10^{-6} \text{ K}^{-1}$. It is usually reinforced with steel rebars that are also isotropic with a CTE of $11,7 \cdot 10^{-6} \text{ K}^{-1}$.

FRP is an anisotropic material therefore its thermal properties depend on the orientation of fibres. CTE in the longitudinal direction (i. e. parallel to the orientation of fibres) depends mostly on the thermal properties of the fibres alone, see equation 3.50 in Chapter 3. For GFRP reinforcement and for the usual FVF around 0,7, the CTE in the longitudinal direction varies around $6 - 10 \cdot 10^{-6} \text{ K}^{-1}$. CTE in the perpendicular

direction however is governed by the properties of the matrix. Considering CTE of individual materials (see Tables 2.5 and 2.4) the resultant CTE of the composite in the perpendicular direction varies around $25 - 50 \cdot 10^{-6} \text{ K}^{-1}$. This is up to 4 times higher than concrete.

The difference of CTE between concrete and the reinforcement causes the rebars to expand and shrink more than the surrounding concrete. This creates transversal strain that causes radial pressure on the concrete surrounding the reinforcement and creates microcracks in the interphase. These microcracks grow in time as the reinforced element is exposed to thermal loading and the bond strength of the rebars is lowered. Longitudinal splitting of concrete cover can be observed.

2.8 Durability under freeze/thaw cycles

Concrete is a permeable material that contains cracks on its surface. To improve the durability to freeze/thaw cycles of concrete, air entraining admixture must be used in the concrete mixture. Dosing the right amount creates closed air bubbles of prescribed diameter, enabling the growth of ice crystals. Water can however accumulate at the interface between the reinforcement and concrete. And if it crystalizes here then it could damage the interface between the two materials.

The durability of GFRP is still largely unknown because it is a relatively new material for civil engineering purposes. It is however more complex than concrete as GFRP is a composite material. The properties of both constituents (fibres and matrix) have to be investigated along with the interface between them. As Ceroni et. al. stated the environments that degrade the polymer resin or the fibre resin interface are also likely to degrade the bond strength of a FRP bar [19].

The resistance of the matrix to high temperatures depends on the thermal properties of the resin, specifically on its glass transition temperature. It varies from $70 \text{ }^\circ\text{C}$ to $175 \text{ }^\circ\text{C}$ [10]. At temperatures above glass transition the bond strength and the ability of the matrix to transfer stresses is sharply reduced [20]. Temperatures below $0 \text{ }^\circ\text{C}$ also have a negative effect on the matrix. Pores in the matrix can cause stress concentration under tensile load (i. e. prestressing force) and this can cause microcracking in the matrix and fibre-matrix degradation [10, 21].

Strong alkaline environment in concrete poses a threat for glass fibres. They are susceptible to hydrolysis – a chemical reaction that breaks down polymer chains [22] causing embrittlement of fibres and damage to the fibre resin interface [20, 19]. This

causes a loss of tensile and interlaminar strengths. The use of alkali-resistant fibres or a correct choice of a matrix can suppress this effect.

According to K. Laoubi [21], freeze/thaw cycles have a similar effect on the interface of GFRP and concrete as freezing water due to the different thermal expansions of FRP and concrete. This can lead to higher transversal strains in GFRP than in concrete causing radial pressure and a possible longitudinal splitting of concrete cover. And when combined with chemical attacks (water and chlorine ions penetrating in concrete), a degradation of fibres, resin and their interface can be observed [19]. This is often solved with prescribed values of the thickness of a concrete cover ranging from 1,5–2 times the diameter of the rebar, depending on the design code and type of reinforcement used (ordinary or prestressed).

Micelli et. al. studied the effects of accelerated ageing by using a combined effect of freeze/thaw cycles, high temperature, high relative humidity and UV radiation on GFRP rods. It was observed that freeze/thaw cycles do not deteriorate the mechanical properties of GFRP considering a proper resin is used. To simulate the environment in concrete, a GFRP rod was exposed in an alkaline solution. But a great decrease of 40 % after 42 days in tensile strength was observed. It was concluded that the use of polyester resin is therefore inapplicable in concrete [20, 19].

Subramaniam et. al. investigated the influence of freeze/thaw cycles on the degradation of the FRP–concrete interface. He used digital image correlation technique to analyze interfacial fracture parameters and shear stress transfer on specimens that were subjected to 100, 200 and 300 freeze/thaw cycles. The temperature changed from 5 °C to -18 °C in one cycle during 12 hours. He concluded that the F/T cycles did not damage the composite sheet used as its elastic modulus remained unchanged. But the interface between the composite sheet and concrete sustained damage because the load bearing capacity of the samples subjected to F/T cycles was lowered. He also observed a decrease in fracture energy as the number of freeze/thaw cycles increased [23].

Laoubi et. al. tested individual and combined effect of sustained bending stress and F/T cycles on continuous GFRP rebars used to reinforce 1,8 m long concrete beams. The beams were subjected to 100, 200 and 360 F/T cycles from 20 °C to -20 °C that simulated the life time of structures in the cold regions of North America. The conditioned beams were tested up to failure in a four-point bending test over a clear span of 1500 mm. The test results showed that the single or coupled effects of F/T cycles and sustained bending stress had no significant effect on the behaviour of the tested beams in terms of deflections, strains and ultimate load bearing capacity [21].

The durability of the FRP–concrete interface and bond strength was tested by Davalos et. al. He used concrete with high strength and several GFRP specimens in a pullout test. Prior to testing a part of the samples were subjected to freeze/thaw cycles from 60 °C to -20 °C for 30 days. The bond failure during pullout was brittle and happened in the interface of the sand coated layer (which is full of the resin) and the core of the bar (which is smooth and does not provide enough friction). Davalos used even a scanning electron microscopy to analyze the interface and found microcracks in concrete. These were probably induced by the shrinking and expanding of the rebar due to the difference in thermal expansions with concrete. About an 18 % of bond strength reduction for glass fibres was observed [24].

Very similar results were obtained by Shi et. al. He tested the effect of freeze/thaw cycles combined with sustained loads on the interface between externally bonded basalt FRP and concrete. He designed special double lap sheer specimens, subjected them to 50, 100, 150 and 200 temperature cycles with temperatures from 20 °C to -25 °C. He observed a degradation of fracture energy, load bearing capacity and compressive strength with the increasing number of freeze/thaw cycles. The effect was even worse when sustained load was applied during the temperature loading [25].

Chapter 3

Numerical approach

This chapter describes numerical modeling on every scale, from micro- to macroscale. Chapter 3.1 deals with micromechanical analysis of GFRP (the mechanical and thermal properties of a GFRP rebar). Chapter 3.2 describes 2D FEM modeling of heat transport through a concrete cross-section on mesoscale. The last chapter 3.3 shows advanced 3D modeling of a concrete beam prestressed with GFRP reinforcement in ATENA software.

3.1 Micromechanical analysis of a lamina

The objective of this chapter is to show various methods that can be used to estimate resultant mechanical properties of a composite material based on the knowledge of the mechanical properties of its constituents. Each method will be presented theoretically, applied on a specific material (GFRP rebar) and the resultant mechanical properties will be presented and compared.

Representative volume element (RVE) is the smallest portion of the material that still represents the macroscopic continuum as a whole. Even though RVE represents a volume of a heterogeneous material (i. e. fibres and matrix), it can be replaced by a homogeneous material without affecting the state of stresses in the composite. Fibre spacing and lamina-thickness are typical RVE dimensions [9].

A *lamina* is one layer of unidirectional fibres embedded in a matrix. The formulas used to calculate the mechanical properties of a lamina are generally more precise when calculating stiffness but unreliable when calculating strength due to numerous facts: the structure of the composite is formed each time as new during production, the properties of fibres and matrix are not always the same, FVF is slightly different or the homogeneity of fibres can be damaged during manufacturing process. All these and many more factors apply so the formulas provide us with *probable* results but not

exact. Exact results can only be obtained by experimental testing of test samples but it is not always possible to fabricate them in the required FVF. Therefore the specimen with a prescribed FVF is tested and the properties of individual constituents are *back-calculated* using the methods presented below. After the basic properties are obtained the formulas can be used to calculate the final properties of the composite with a *different FVF*.

GFRP is a transversally isotropic material. It has a plane of symmetry, where its properties are isotropic (axis 2,3) and parallel to it is the direction of anisotropy (axis 1). Due to this its mechanical properties are described only by 5 independent material constants: E_1 , E_2 , G_1 , G_2 and ν_{12} .

3.1.1 Basic properties

When designing a composite material, the designer has to specify the individual constituents (i. e. fibres and matrix), their relative amount (described by fibre or mass volume fraction) and the geometry of the product simultaneously.

Fibre volume fraction (FVF) describes the volumetric amount of fibres in the composite. FVF is determined by the manufacturing process. It can be defined by:

$$V_f = \frac{v_f}{v_c} = \frac{A_f}{A_c} \quad (3.1)$$

Where: v_f – volume of fibres in the composite

v_c – volume of the composite

A_f – area of the fibres

A_c – area of the composite

Matrix volume fraction (MVF) defines the amount of matrix by volume in the composite. It is defined by:

$$V_m = \frac{v_m}{v_c} = \frac{A_m}{A_c} \quad (3.2)$$

Where: v_m – volume of fibres in the composite

A_m – area of the matrix

The total volume of the composite is the sum of volume of fibres and the matrix:

$$1 = V_f + V_m \quad (3.3)$$

$$v_c = v_f + v_m \quad (3.4)$$

Mass fractions are used in production because it is easier to weight the constituents that to determine their volume fraction.

Weight of fibres can be defined by:

$$W_f = \frac{w_f}{w_c} \quad (3.5)$$

Where: w_f – mass of fibres in the composite

w_c – mass of the composite

Weight of matrix is defined by:

$$W_m = \frac{w_m}{w_c} \quad (3.6)$$

Where: w_m – mass of matrix in the composite

The total mass of the composite is the sum of masses of fibres and matrix:

$$1 = W_f + W_m \quad (3.7)$$

$$w_c = w_f + w_m \quad (3.8)$$

Volume and mass fractions are linked together by the following equations:

$$W_f = \frac{\rho_f}{\rho_c} \cdot V_f \quad (3.9)$$

$$W_m = \frac{\rho_m}{\rho_c} \cdot V_m \quad (3.10)$$

Density of any material can be calculated as mass divided by volume, or:

$$\rho_c = \sum_{i=1}^n \rho_i \cdot V_i = \rho_f \cdot V_f + \rho_m \cdot V_m \quad (3.11)$$

$$\frac{1}{\rho_c} = \sum_{i=1}^n \frac{W_i}{\rho_i} = \frac{W_f}{\rho_f} + \frac{W_m}{\rho_m} \quad (3.12)$$

Where: $\rho_{c,f,m}$ – density of composite, fibres or matrix respectively

Volume and mass fractions are linked together by the following equations:

$$W_i = \frac{\rho_i}{\rho_c} \cdot V_i$$

$$W_f = \frac{\rho_f}{\rho_c} \cdot V_f \tag{3.13}$$

$$W_m = \frac{\rho_m}{\rho_c} \cdot V_m \tag{3.14}$$

Voids can appear in the matrix during the manufacturing process of the composite material. They deteriorate its properties, lowering strength, stiffness, fatigue and moisture resistance [12]. The presence of voids is signaled when comparing two densities (one experimentally measured and the other calculated via previous equations). If they differ, than *volume void content* can be calculated by:

$$V_v = \frac{\rho_c - \rho_{c,exp}}{\rho_c} \tag{3.15}$$

3.1.2 Strength of material approach

A. Kaw. [12] defines the following assumptions that play a key role in the *strength of materials* approach model. These assumptions enable us to replace the heterogeneous material in the RVE by a homogeneous one while satisfying the compatibility of displacements with the rest of the macroscopic continuum [9]:

- the bond between fibres and matrix is perfect
- the elastic moduli, diameters and space between fibres are uniform
- fibres are continuous and parallel
- fibres possess uniform strength
- fibres and matrix follow Hooke’s law (linear elastic behavior) and are isotropic
- the composite is free of voids

In the following text various indexes are used. *1* stands for the direction parallel to the orientation of fibres (axis 1). *2* stands for the direction perpendicular to the orientation of fibres (axis 2 or 3). *c,f,m* stands for composite, fibres and matrix respectively.

Longitudinal elastic modulus E_1 : RVE is stretched by stress σ_1 , resulting in a elongation ΔL along the fibre direction (axis 1, see Figure 3.1). Based by the assumptions mentioned above the matrix and fibres will elongate by the same amount.

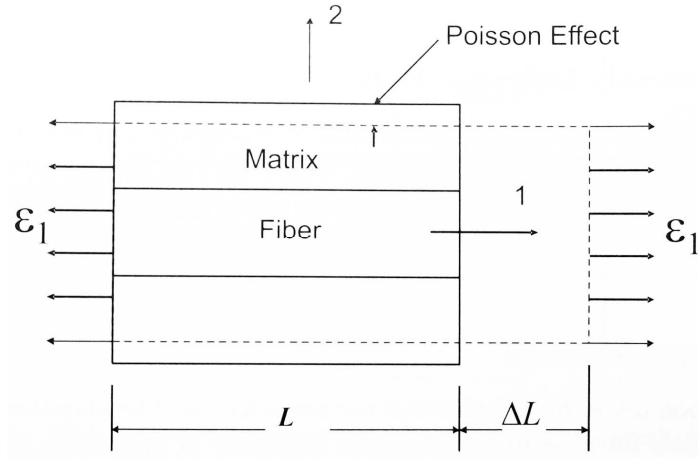


Figure 3.1: Determining elastic modulus on RVE [9]

Basic assumption for the calculation of a longitudinal elastic modulus:

$$\epsilon_c = \epsilon_f = \epsilon_m \quad (3.16)$$

Strain by definition:

$$\epsilon_1 = \frac{\Delta L}{L} \quad (3.17)$$

Fibres (in this case glass) and matrix are isotropic, Hooke's law applies:

$$\sigma_f = E_f \cdot \epsilon_1 \quad (3.18)$$

$$\sigma_m = E_m \cdot \epsilon_1 \quad (3.19)$$

The whole area of the cross-section is:

$$A = A_f + A_m \quad (3.20)$$

The stress σ_1 is distributed evenly:

$$\sigma_1 \cdot A = \sigma_f \cdot A_f + \sigma_m \cdot A_m \quad (3.21)$$

Using equation (3.1) and (3.2) we obtain:

$$\sigma_1 = \epsilon_1 \cdot (E_f \cdot V_f + E_m \cdot V_m) \quad (3.22)$$

Hooke's law for a homogeneous material:

$$\sigma_1 = E_1 \cdot \epsilon_1 \quad (3.23)$$

Combining equations (3.22) and (3.23) we get:

$$E_1 = E_f \cdot V_f + E_m \cdot V_m \quad (3.24)$$

Slightly modifying the equation (3.24) we get a well known formula – *the rule of mixtures*:

$$E_1 = E_f \cdot V_f + E_m \cdot (1 - V_f) \quad (3.25)$$

Transversal elastic modulus E_2 : RVE is loaded by stress σ_2 in the direction perpendicular to the orientation of fibres. To maintain equilibrium in the transverse direction the stress in the matrix and fibres is the same.

Basic assumption for the calculation of a longitudinal elastic modulus:

$$\sigma_c = \sigma_f = \sigma_m \quad (3.26)$$

Strain, however, acts over a portion of RVE and can be calculated as follows:

$$\varepsilon_2 = \varepsilon_f \cdot V_f + \varepsilon_m \cdot V_m \quad (3.27)$$

Hooke's law applies for the isotropic materials, i. e. fibres and matrix respectively:

$$\varepsilon_f = \frac{\sigma_2}{E_f} \quad (3.28)$$

$$\varepsilon_m = \frac{\sigma_2}{E_m} \quad (3.29)$$

Applying Hooke's law on ε_2 , and combining equations (3.26), (3.27), (3.28) and (3.29), we obtain the following equation called *inverse rule of mixture*:

$$\frac{1}{E_2} = \frac{V_f}{E_f} + \frac{V_m}{E_m} \quad (3.30)$$

Equation (3.30) provides a lower bound for the transversal elastic modulus, the property is underestimated. It can be used for qualitative evaluation of different candidate materials but not for design calculations [9].

In-plane Poisson's ratio ν : is defined as a negative ratio of the normal strain in the transverse direction to the normal strain in the longitudinal direction. RVE is loaded in the axial direction (see Figure 3.1).

Poisson's ratio is then defined as:

$$\nu_{ij} = -\frac{\nu_j}{\nu_i} \quad (3.31)$$

The load is applied in the i -direction, strain is induced by Poisson's effect on the perpendicular (j -) direction. Using the *rule of mixture* (equation 3.25) in the *strength of materials* approach, in-plane Poisson's ratio is defined as:

$$\nu_{12} = \nu_f \cdot V_f + \nu_m \cdot V_m \quad (3.32)$$

The *rule of mixture* provides an approximate prediction of the value which is sufficient for the design of the composite, because the values of ν_f and ν_m are pretty close together.

In-plane shear modulus G : there are three possible approaches:

1. *inverse rule of mixture* provides the following equation for the in-plane shear modulus:

$$\frac{1}{G_{12}} = \frac{V_f}{G_f} + \frac{V_m}{G_m} \quad (3.33)$$

or it can be rewritten as follows:

$$G_{12} = \frac{G_m}{V_m + V_f \cdot G_m/G_f} \quad (3.34)$$

We obtain slightly different results, if we consider that fibres are much stiffer than matrix ($G_f \gg G_m$), then in-plane shear modulus can be approximated by the matrix-dominated approximation:

$$G_{12} \cong \frac{G_f}{1 - V_f} \quad (3.35)$$

2. *cylindrical assemblage model* yields another possible approximation:

$$G_{12} = G_m \cdot \left(\frac{(1 + V_f) + (1 - V_f) \cdot G_m/G_f}{(1 - V_f) + (1 + V_f) \cdot G_m/G_f} \right) \quad (3.36)$$

If $G_f \gg G_m$, the matrix-dominated approximation is:

$$G_{12} \cong G_f \cdot \left(\frac{1 + V_f}{1 - V_f} \right) \quad (3.37)$$

3. *periodic microstructure model* provides another possible formula:

$$G_{12} = G_m \cdot \left(1 + \frac{V_f \cdot (1 - G_m/G_f)}{G_m/G_f + S_3 \cdot (1 - G_m/G_f)} \right) \quad (3.38)$$

where:

$$S_3 = 0,49247 - 0,47603 \cdot V_f - 0,02748 \cdot V_f^2 \quad (3.39)$$

then matrix dominated PMM formula can be written as:

$$G_{12} \cong G_f \cdot \left(1 + \frac{V_m}{G_m/G_f + S_3} \right) \quad (3.40)$$

For isotropic materials (such as matrixes or glass fibres), the shear modulus can be calculated using elastic modulus E and Poisson's ratio ν :

$$G = \frac{E}{2 \cdot (1 + \nu)} \quad (3.41)$$

On the other hand, transversally isotropic materials such as carbon or aramid fibres have five material constants: E_1, E_2, G_1, G_2, ν .

Longitudinal coefficient of thermal expansion α_1 : when a change in temperature ΔT (a difference between actual temperature T and initial temperature T_0) occurs, the original dimensions of the material change in proportion to the temperature change. The coefficient of thermal expansion is then defined as a change in dimension per unit length per unit of temperature.

Consider a lamina loaded with temperature change ΔT . Strain in the lamina is equal for fibres and matrix due to compatibility conditions:

$$\varepsilon_L = \varepsilon_f = \varepsilon_m \quad (3.42)$$

Strain in the individual components can be calculated as:

$$\varepsilon_f = \varepsilon_{el} + \varepsilon_{temp} = \frac{\sigma_f}{E_f} + \alpha_f \cdot \Delta T \quad (3.43)$$

$$\varepsilon_m = \varepsilon_{el} + \varepsilon_{temp} = \frac{\sigma_m}{E_m} + \alpha_m \cdot \Delta T \quad (3.44)$$

Overall force in the longitudinal direction carried by the lamina is zero:

$$F_1 = \sigma_1 \cdot V_c = \sigma_f \cdot V_f + \sigma_m \cdot V_m = 0 \quad (3.45)$$

Stresses in the fibres and matrix are not zero, but:

$$\sigma_f = E_f \cdot (\varepsilon_f - \alpha_f \cdot \Delta T) \quad (3.46)$$

$$\sigma_m = E_m \cdot (\varepsilon_m - \alpha_m \cdot \Delta T) \quad (3.47)$$

Combining equations (3.42), (3.47) and (3.47) into (3.45) we get:

$$\varepsilon_L = \frac{\alpha_f \cdot E_f \cdot V_f + \alpha_m \cdot E_m \cdot V_m}{E_f \cdot V_f + E_m \cdot V_m} \cdot \Delta T \quad (3.48)$$

Considering:

$$\varepsilon_L = \alpha_1 \cdot \Delta T \quad (3.49)$$

We obtain the equation for the *longitudinal coefficient of thermal expansion*:

$$\alpha_1 = \frac{\alpha_f \cdot E_f \cdot V_f + \alpha_m \cdot E_m \cdot V_m}{E_f \cdot V_f + E_m \cdot V_m} \quad (3.50)$$

Using equation (3.24), then equation (3.50) can be rewritten as:

$$\alpha_1 = \left(\frac{\alpha_f \cdot E_f}{E_1} \right) \cdot V_f + \left(\frac{\alpha_m \cdot E_m}{E_1} \right) \cdot V_m \quad (3.51)$$

Transversal coefficient of thermal expansion α_2 :

Transversal strain of fibres and matrix can be calculated as:

$$\varepsilon_T = \varepsilon_{el} + \varepsilon_{temp}$$

$$\varepsilon_{temp,i} = \alpha_{T,i} \cdot \Delta T \quad (3.52)$$

$$\varepsilon_{T,f} = -\nu_f \cdot \frac{\sigma_f}{E_f} + \alpha_f \cdot \Delta T \quad (3.53)$$

$$\varepsilon_{T,m} = -\nu_m \cdot \frac{\sigma_m}{E_m} + \alpha_m \cdot \Delta T \quad (3.54)$$

Rule of mixtures defines ε_T as:

$$\varepsilon_T = V_f \cdot \varepsilon_{T,f} + V_m \cdot \varepsilon_{T,m} \quad (3.55)$$

Substituting equations (3.54) and (3.54) into (3.55) we get:

$$\begin{aligned} \varepsilon_T = & - (V_f \cdot \nu_f + V_m \cdot \nu_m) \cdot \varepsilon_L + \\ & + (V_f \cdot \nu_f \cdot \alpha_f + V_m \cdot \nu_m \cdot \alpha_m) \cdot \Delta T + \\ & + (V_f \cdot \alpha_f + V_m \cdot \alpha_m) \cdot \Delta T \end{aligned} \quad (3.56)$$

Where:

$$\varepsilon_L = \frac{\alpha_f \cdot V_f \cdot E_f + \alpha_m \cdot V_m \cdot E_m}{V_f \cdot E_f + V_m \cdot E_m} \cdot \Delta T \quad (3.57)$$

Substituting equations (3.53) and (3.57) into (3.56) we get the equation for the *transversal coefficient of thermal expansion* [26]:

$$\alpha_2 = V_f \cdot \alpha_f + V_m \cdot \alpha_m + \frac{\nu_m \cdot E_f - \nu_f \cdot E_m}{\frac{E_f}{V_m} + \frac{E_m}{V_f}} \cdot (\alpha_m - \alpha_f) \quad (3.58)$$

Autar Kaw [12] even provides a formula that can be used to estimate the *ultimate tensile strength* of the composite based on the mechanical properties of the constituents. It must be noted that the prediction of the ultimate tensile strength is unprecise due to the fact that strength of the composite depends not only on the properties of the constituents but on other factors such as material and geometric nonhomogeneities, fibre-matrix interface, fabrication process and environment [12].

$$\sigma_{1,ult} = \sigma_{f,ult} \cdot V_f + \varepsilon_{f,ult} \cdot E_m \cdot V_m \quad (3.59)$$

where:

$$\varepsilon_{f,ult} = \frac{\sigma_{f,ult}}{E_f} \quad (3.60)$$

3.1.3 Semi-empirical approach by Halpin–Tsai

Inverse rule of mixture (used in equations for transversal elastic modulus E_T and in-plane shear modulus G) provides results that do not correspond very well with experimental data, therefore more advanced techniques must be employed. These techniques include numerical methods such as finite element method, finite difference and boundary element methods, elasticity solution and variational principal models [12].

The methods mentioned above may provide more accurate results but they require complex calculations not suitable for quick and precise estimations at the same time. Thus *semi-empirical models* have been developed and tested on data from experiments. *Halpin–Tsai* approach is based on the *self-consistent method* presented by Hill [27], but provides a more precise approximation compared to *strength of material approach*. Halpin–Tsai model presents a simple analytical form that can be used to estimate properties of composite materials with a broad range of reinforcement geometries that are suitable for designing composites.

Longitudinal elastic modulus E_1 : is the same as in *strength of material approach*, which provides accurate results:

$$E_1 = E_f \cdot V_f + E_m \cdot V_m \quad (3.61)$$

Transversal elastic modulus E_2 : is calculated by the following formula[12]:

$$E_2 = E_m \cdot \frac{1 + V_f \cdot \eta \cdot \xi}{1 - V_f \cdot \eta} \quad (3.62)$$

Where:

$$\eta = \frac{(E_f/E_m) - 1}{(E_f/E_m) + \xi} \quad (3.63)$$

and ξ is the reinforcement factor, which depends on:

- fibre geometry
- packing geometry
- loading conditions

Halpin and Tsai [28] deducted ξ from experiments and for example for a fibre geometry of circular fibers in a packing geometry of a square array (case of GFRP) $\xi = 2$.

In-plane Poisson's ratio ν : is the same as in *strength of material approach*:

$$\nu_{12} = \nu_f \cdot V_f + \nu_m \cdot V_m \quad (3.64)$$

In-plane shear modulus G : can be obtained from the following equation:

$$G_{12} = G_m \cdot \frac{1 + V_f \cdot \eta \cdot \xi}{1 - V_f \cdot \eta} \quad (3.65)$$

Where:

$$\eta = \frac{(G_f/G_m) - 1}{(G_f/G_m) + \xi} \quad (3.66)$$

and the reinforcement factor ξ again depends on fibre geometry, packing conditions and loading conditions. For circular fibers in a square array, $\xi = 1$. This works only for FVF up to 0,5. When the FVF is higher, a modification (suggested by Hewitt and Malherbe [29]) of ξ must be applied:

$$\xi_{FVF>0,5} = 1 + 40 \cdot V_f^{10} \quad (3.67)$$

Longitudinal coefficient of thermal expansion α_1 : same as in *strength of materials approach*:

$$\alpha_1 = \frac{\alpha_f \cdot E_f \cdot V_f + \alpha_m \cdot E_m \cdot V_m}{E_f \cdot V_f + E_m \cdot V_m} \quad (3.68)$$

Transversal coefficient of thermal expansion α_2 : same as in *strength of materials approach*:

$$\alpha_2 = V_f \cdot \alpha_f + V_m \cdot \alpha_m + \frac{\nu_m \cdot E_f - \nu_f \cdot E_m}{\frac{E_f}{V_m} + \frac{E_m}{V_f}} \cdot (\alpha_m - \alpha_f) \quad (3.69)$$

3.1.4 Mori–Tanaka approach

Mori–Tanaka method is one of analytical mean-field homogenization schemes. Based on linear elasticity it can be used to explicitly predict elastic properties of multi-phase composite materials. It considers elliptical inclusions in an infinite matrix.

To obtain the resultant macroscopic properties, i. e. deduce macroscopic strain and stress fields from microscopic fields, a two step process is necessary. This problem cannot be explicitly solved but leads to an estimate. During the first step an isolated local inclusion is embedded in an infinite matrix and solved to get local field approximation as in Eshelby's text [30]. Local fields are then averaged in the next step to obtain a macroscopic response [31].

Macroscopic strain and stress fields are linked to microscopic fields by concentration factors. Considering Eshlebian *concentration factor* for ellipsoidal inclusions (circular cylinders) in an infinite matrix [32]:

$$\mathbf{T}_r = [\mathbf{I} - \mathbf{P} (\mathbf{L}_1 - \mathbf{L}_2)]^{-1} \quad (3.70)$$

Where: \mathbf{P} – matrix based on the type of inclusion

\mathbf{L}_i – stiffness matrix of the matrix (1) or fibres (2)

Stiffness matrix of the composite can then be calculated as [32]:

$$\mathbf{L}_{\text{comp}} = \left[\sum_{i=1}^2 c_i \mathbf{L}_i \mathbf{T}_r \right] \left[\sum_{i=1}^2 c_i \mathbf{T}_r \right]^{-1} \quad (3.71)$$

and in my specific case:

$$\mathbf{L}_{\text{comp}} = [c_1 \mathbf{L}_1 \mathbf{I} + c_2 \mathbf{L}_2 \mathbf{T}_r] [c_1 \mathbf{I} + c_2 \mathbf{T}_r]^{-1} \quad (3.72)$$

Where: c_i – volume fraction

\mathbf{L}_i – stiffness matrix of the matrix (m) or fibres (f)

\mathbf{T}_r – concentration factor

First, the local compliance matrix for each material is calculated and then inverted to obtain stiffness matrix for each constituent. The shape of the inclusion is then considered and the respective \mathbf{P} matrix calculated. Then the procedure follows the suggested procedure as the concentration factor \mathbf{T}_r is calculated, followed by the stiffness matrix for the homogenized composite rebar. Stiffness matrix is then inverted to obtain compliance matrix and the respective properties are back-calculated from their respective positions.

3.1.5 Comparison of results

Specific material properties for the GFRP rebars (see Table 3.1) were either measured in the Experimental centre or provided by the manufacturer (Prefa kompozit, a.s.). These were then used as input data for the calculation of resultant mechanical properties using the *Strength of material* approach, *Halpin-Tsai* approach and *Mori-Tanaka* homogenization (see Table 3.2 for results):

Table 3.1: Material properties of GFRP constituents, FVF = 0,58

	Tensile strength [MPa]	Elastic modulus [GPa]	Shear modulus [GPa]	Poisson's ratio [-]	CTE ·10 ⁻⁶ [K ⁻¹]
AR glass fibre	750	73	29,9	0,22	6,5
Vinyl ester matrix	82,7	3,4	1,2	0,38	50

Several methods were used to obtain the resultant properties of the composite rebar. But as it can be seen and regardless of method used, the properties do not differ too much. It is therefore possible to use even the simplest method – the *strength of materials* approach to get sufficient results.

Calculated properties will be used for the numerical model of the prestressed reinforcement in ATENA software. ATENA does not contain a model for a composite reinforcement. But steel reinforcement can be modified accordingly as described in the respective chapter.

Table 3.2: Calculated resultant properties of the composite rebar

	Elastic modulus <i>longitudinal</i> [GPa]	Elastic modulus <i>transversal</i> [GPa]	Shear modulus [GPa]	Poisson's ratio [-]	CTE <i>longitudinal</i> $\cdot 10^{-6}$ [K ⁻¹]	CTE <i>transversal</i> $\cdot 10^{-6}$ [K ⁻¹]	Tensile strength [MPa]
Strength of material approach	43,77	7,61	2,77 4,06 4,09	0,29	7,92	21,20	449,67
Halpin-Tsai approach	43,77	13,84	4,26	0,29	7,92	21,20	-
Mori-Tanaka approach	43,80	10,93	3,67	0,28	-	-	-

3.2 Modeling of heat transfer in MATLAB

The objective of this chapter was to investigate the distribution of temperature on the concrete beam cross-section throughout the prescribed temperature loading. There were concerns that the temperature does not affect the rebar long enough as a 20 mm thick layer of concrete cover protects it. A change of temperature (throughout the freeze/thaw cycles) should cause the rebar to shrink and expand more than the surrounding concrete due to the different CTE.

A model of non-stacionary heat transfer in concrete was programmed in MATLAB to predict and verify the distribution of temperature throughout the freeze/thaw cycle. The duration of the cycle was then modified to make sure the temperature reaches the rebar and affects it long enough to shrink or expand. The model was then compared with the same model in a different software – TRFEL (stands for TRansport Finite ELelements).

TRFEL is an open source individual module developed for transport problems at the Department of Mechanics at Civil Engineering Faculty of ČVUT. The results of this software were already verified on many practical applications so it should provide an accurate approximation. The accuracy of both models depends on input parameters that could not be exactly specified as they depend on a number of factors. These parameters were then estimated according to previous experiments and the results then confronted with the measurements from thermometers that were placed in the beams, as described in Chapter 4.

3.2.1 Non-stationary heat transfer

Non-stationary heat transfer is governed by the following partial differential equation. It describes the distribution of temperature in an area over time:

$$\frac{\partial}{\partial x} \left(\lambda \frac{\partial T}{\partial x} \right) + \frac{\partial}{\partial y} \left(\lambda \frac{\partial T}{\partial y} \right) = \rho c \frac{\partial T}{\partial t} \quad (3.73)$$

Where: λ – thermal conductivity

T – temperature

ρ – density

c – specific heat

with the following Cauchy's mixed boundary condition:

$$\bar{q}(\mathbf{x}) = \alpha(\mathbf{x})(T(\mathbf{x}) - T_0(\mathbf{x})) \quad (3.74)$$

Where: \bar{q} – transfer of flux on the boundary

α – transfer coefficient

T – unknown temperature in the domain

T_0 – prescribed outside temperature

Since it is almost impossible to solve this equation analytically it is necessary to employ a numerical method. One of the most frequently used is *finite element method*. This is due to the fact that it can be easily implemented in computer software. The following procedure was taken from [33].

Finite element method only approximates the solution of the differential equation with a certain difference, or residuum. The residuum is then minimized by *variation principles* or *Galerkin method* of weighted residuals (which will be further used). Differential equation along with boundary conditions is called the *strong form* of the problem [34]. The *weak form* is the integral part of this problem [34], i. e. a weight (or test) function (w) is applied on the governing equation:

$$\int_{\Omega} w \left(\rho c \frac{\partial T}{\partial t} - \frac{\partial}{\partial x} \left(\lambda \frac{\partial T}{\partial x} \right) - \frac{\partial}{\partial y} \left(\lambda \frac{\partial T}{\partial y} \right) \right) d\Omega = 0 \quad (3.75)$$

Applying Galerkin method for domain discretization and Green theorem we obtain the following equation in matrix form, where time is considered constant:

$$\mathbf{P} \frac{\partial \mathbf{T}}{\partial t} + \mathbf{H} \mathbf{T} = \mathbf{f} \quad (3.76)$$

Where: \mathbf{P} – matrix of heat capacity

\mathbf{H} – matrix of thermal conductivity

\mathbf{T} – column matrix of unknown temperatures

\mathbf{f} – column matrix of heat transfer on the boundary

Time discretization can be performed *analytically* (by frequency response procedure or modal decomposition analysis), using *finite difference method* (which was used in the following procedure) or *Galerkin method* of weighted residuals.

The unknown temperature field was approximated on an interval $[t, t + \Delta t]$ using

Crank–Nicolson implicit method (that is unconditionally stable), and using $\tau = 0,5$:

$$\mathbf{T} = (1 - \tau) \mathbf{T}_t + \tau \mathbf{T}_{t+\Delta t}, \quad \tau \in [0, 1] \quad (3.77)$$

and the same with matrix of heat transfer on the boundary:

$$\mathbf{f} = (1 - \tau) \mathbf{f}_t + \tau \mathbf{f}_{t+\Delta t}, \quad \tau \in [0, 1] \quad (3.78)$$

When applied on the time derivation we get:

$$\frac{\partial T}{\partial t} = \frac{1}{\Delta t} (\mathbf{T}_{t+\Delta t} - \mathbf{T}_t) \quad (3.79)$$

Substituting equations (3.77), (3.78), (3.79) into (3.76) and after a few modifications using Crank–Nicolson $\tau = 0,5$ we get:

$$\mathbf{C} \mathbf{T}_{t+\Delta t} = \mathbf{D} \mathbf{T}_t + \mathbf{A} \quad (3.80)$$

where:

$$\mathbf{C} = \frac{1}{2} \mathbf{H} + \frac{1}{\Delta t} \mathbf{P} \quad (3.81)$$

$$\mathbf{D} = -\frac{1}{2} \mathbf{H} + \frac{1}{\Delta t} \mathbf{P} \quad (3.82)$$

$$\mathbf{A} = \frac{1}{2} (\mathbf{f}_t + \mathbf{f}_{t+\Delta t}) \quad (3.83)$$

3.2.2 Implementation in MATLAB

The above mentioned algorithm was implemented in MATLAB software. It was written in the way that in the beginning a few input values are needed, the programme then calculates the temperature field over the cross-section and prints out graphs showing the temperature field in the requested time step.

The input parameters that were necessary to specify include (see Table 3.3 and Figure 3.2):

- dimensions of the cross-section
- number of finite elements in each direction of the 2D domain

- material constants (density, specific heat, thermal conductivity)
- constants defining boundary conditions (transfer coefficient, temperature at the beginning of the freeze/thaw cycle)
- time function describing a temperature change during freeze/thaw cycle

Table 3.3: Input parameters for MATLAB

	Symbol	Value	
Density	ρ	2 250	[kg m ⁻³]
Specific heat	c	1 020	[J kg ⁻¹ K ⁻¹]
Thermal conductivity	λ	1,5	[W m ⁻¹ K ⁻¹]
Transfer coefficient	α	20	[J m ⁻² K ⁻¹ s ⁻¹]

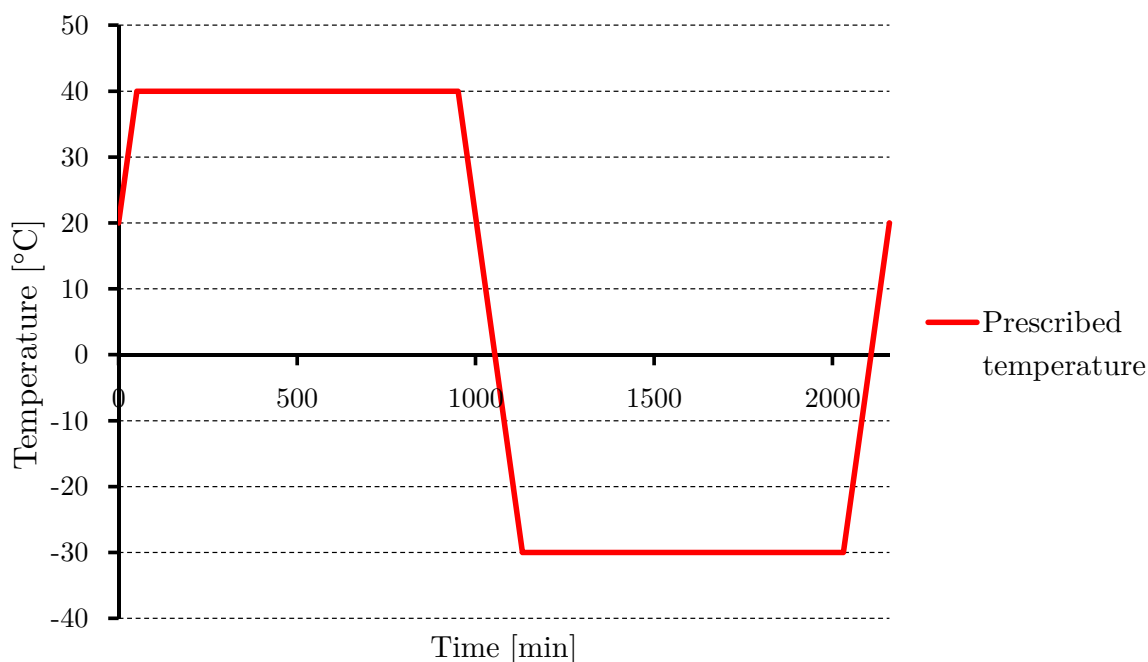


Figure 3.2: Prescribed freeze/thaw cycle

Based on the input values, the programme then generates the mesh over the 2D domain using triangular elements with linear base functions. The border elements with their respective sides (as borders) are automatically located and the transfer of flux is assigned on them. This way the column matrix of heat transfer is calculated. Next the matrix of heat capacity and thermal conductivity are localized in the global matrixes and the temperature field is calculated. The calculation is performed in sequential steps. Step length was 1 minute in order to obtain precise results.

3.2.3 Results of heat transfer modeling

Temperature cycle is described in greater detail in Chapter 4 but it is necessary at least to mention the important points that describe it. Initial temperature was 20 °C at the beginning of the freeze/thaw cycle (see Figure 3.3). After 51 minutes it was raised to 40 °C.

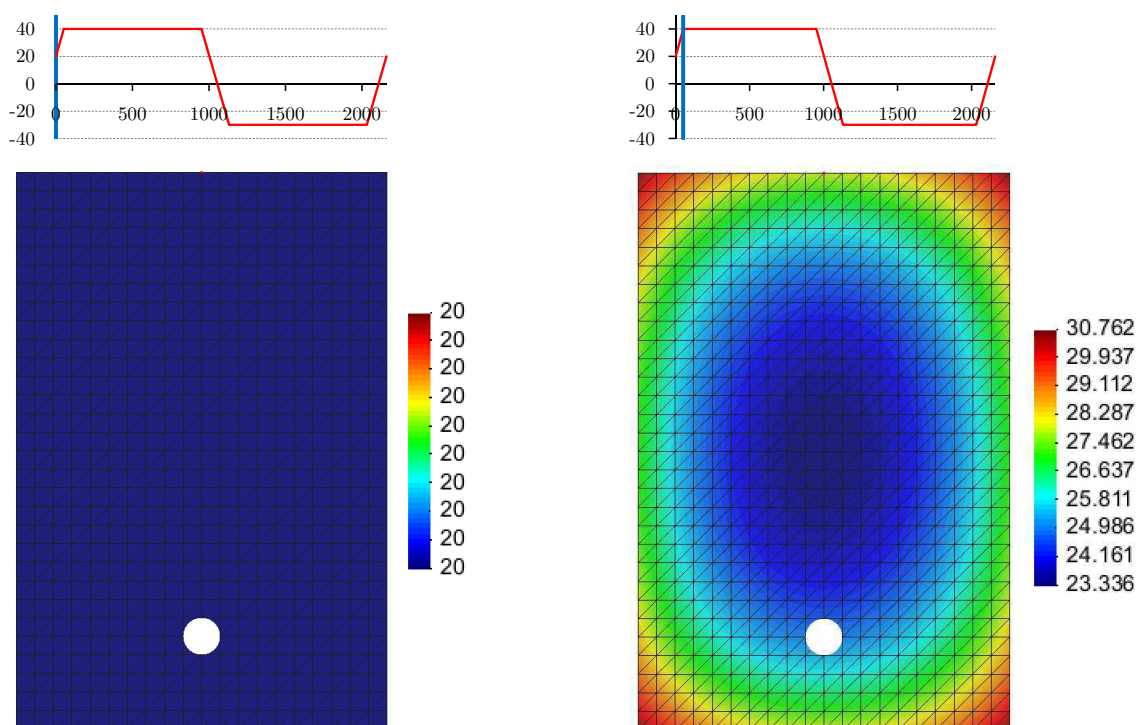


Figure 3.3: Temperature field over the cross-section in the beginning of the freeze/thaw cycle (left) and after 51 minutes (right)

After that the temperature was kept constant at 40 °C for 15 hours (= 951 minutes in total). The temperature then equalized throughout the cross-section. After there was a decrease in temperature prescribed, from 40 °C to -30 °C in just 3 hours (= 1131 minutes in total), as it can be seen on Figure 3.4.

The temperature was then kept constant at -30 °C for 15 hours (= 2031 minutes in total). From there the temperature raised with the same gradient (as was used to cool the cross-section) to reach 20 °C in 129 minutes (= 2160 minutes in total). The total duration of the freeze/thaw cycle was 36 hours (= 2160 minutes).

Figure 3.6 shows the temperature in the center of gravity of the GFRP rebar (center of the white “dot”), located 24,5 mm from the outer surface of the concrete. Because the temperature throughout the concrete cross-section copied the prescribed temperature “fast” enough, this cycle was accepted and used for the testing of concrete specimens in the climatic chamber.

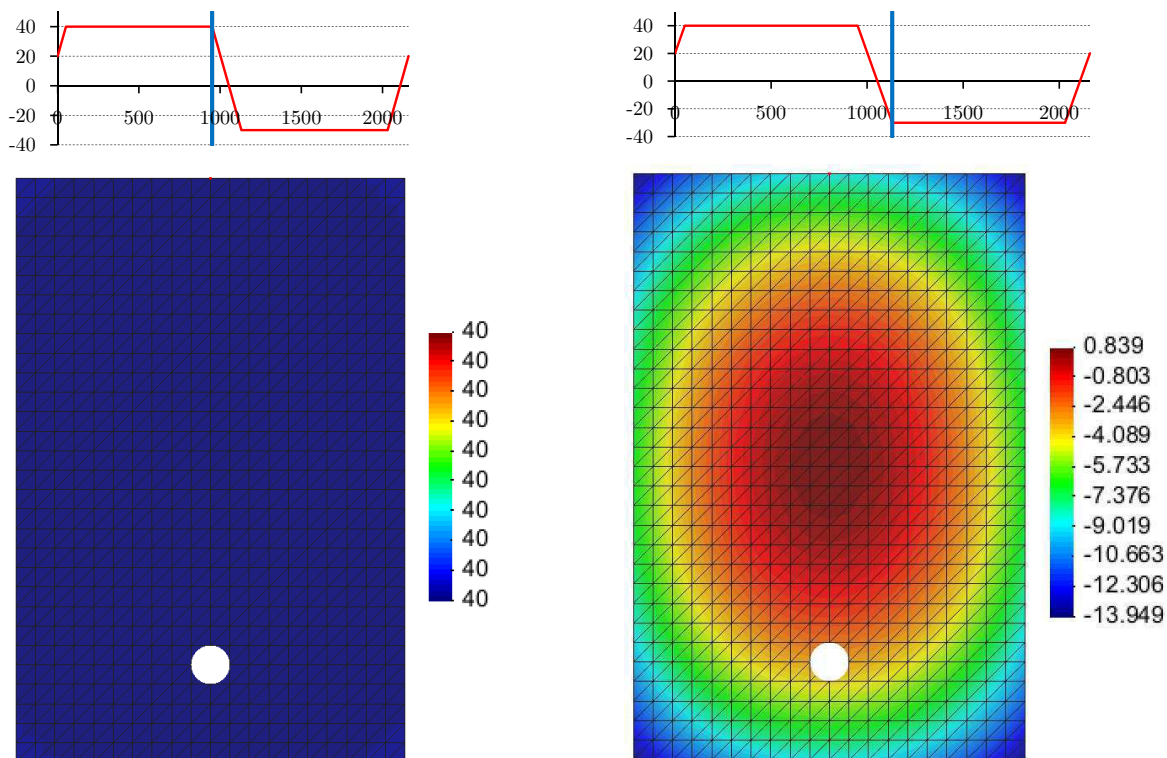


Figure 3.4: Temperature field over the cross-section after 951 minutes (left) and after 1131 minutes (right)

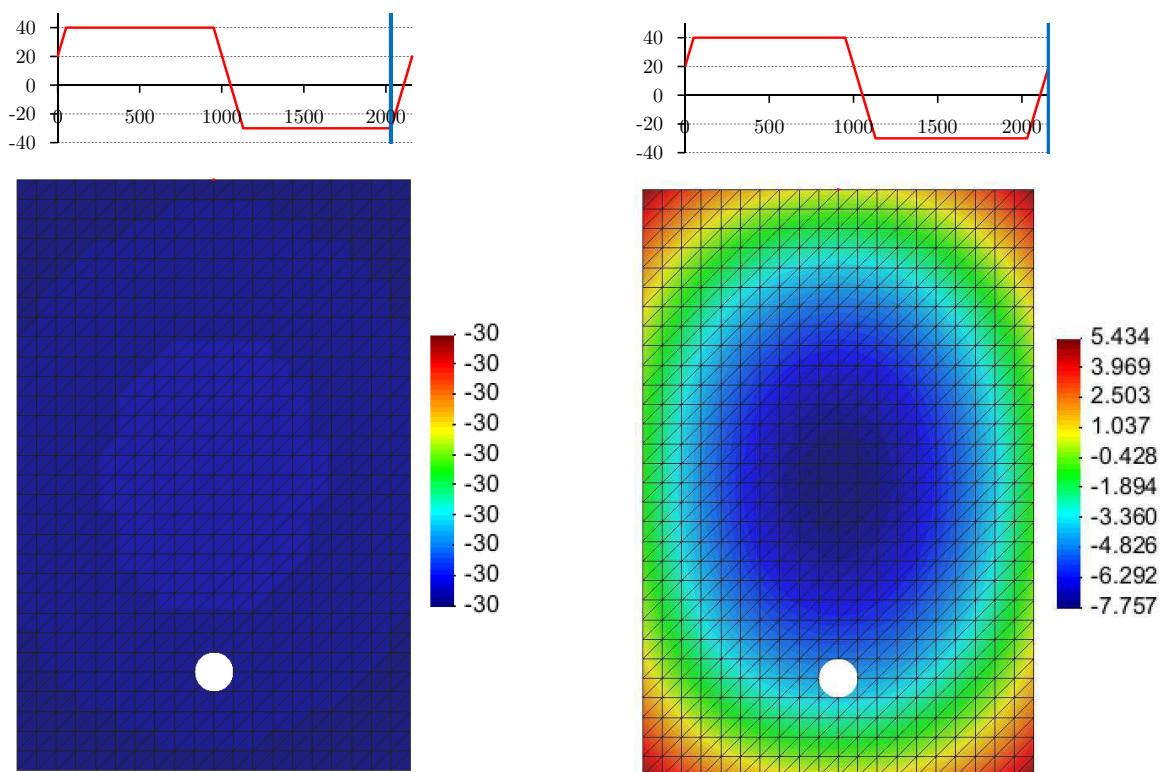


Figure 3.5: Temperature field over the cross-section after 2031 minutes (left) and after 2160 minutes (right)

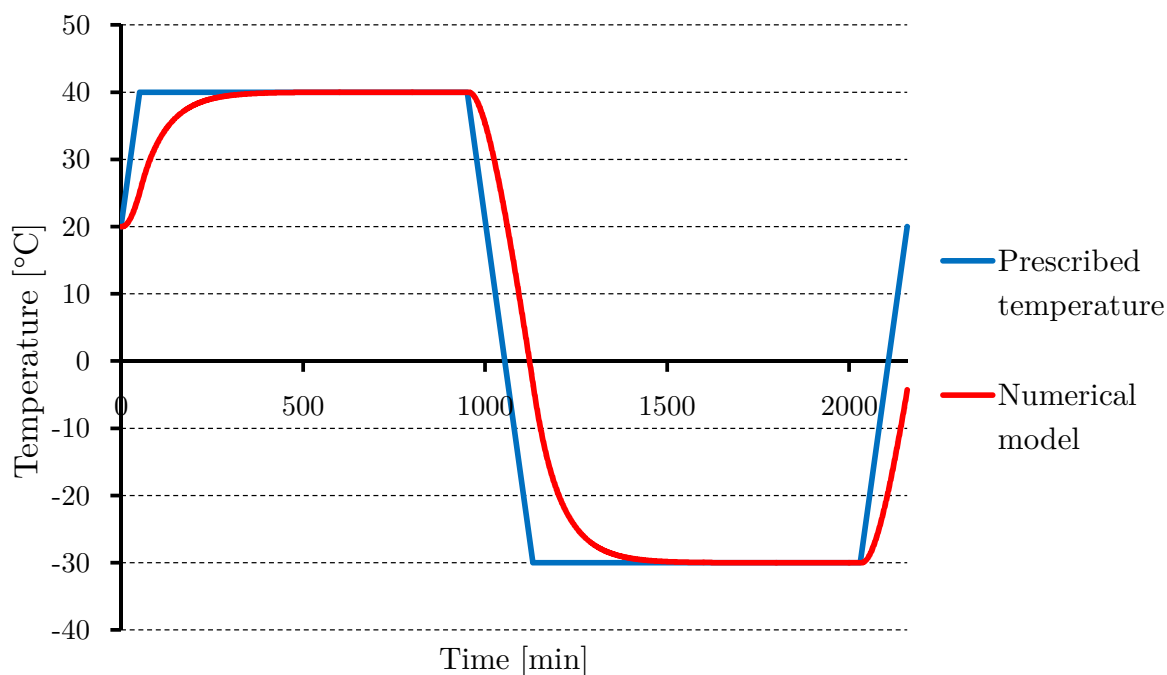


Figure 3.6: Temperature at GFRP rebar during freeze/thaw cycle

3.3 Nonlinear analysis in ATENA

The objective of this chapter was to design a numerical model that can be used to predict the behaviour of GFRP reinforced concrete beams. Because traditional FEM-based software does not allow to use different material models for reinforcement other than steel, an advanced software was used. ATENA (stands for Advanced Tool for Engineering Nonlinear Analysis) was developed by Červenka Consulting Ltd. in order to simulate and predict real structural behaviour of reinforced concrete structures. It considers cracking and crushing of concrete and yielding of steel reinforcement. It is therefore possible to check strongly reinforced details such as D-regions in structures.

In my case it was chosen because it enables the user to fully modify the material models for both concrete and reinforcement based on the actual results of real experiments. In this way the model can be optimized to predict the behaviour before the actual specimens testing takes place. It can be used to calculate stresses, crack location and widths, deflection at any point along with the load bearing capacity of the beams. It can save valuable time that the production and testing of concrete samples takes.

Modeling consists of three phases: preprocessing, computing and postprocessing. Preprocessing was done in GiD software that provides a user-friendly interface for the preparation of a model. It is possible to generate the geometry, assign material models,

loads and generate mesh. It then generates an input file that is automatically loaded into ATENA and calculated. During calculation it is possible to visualize stresses, deformation of the model and cracks, monitor requested values and generate graphs. Once the calculation is complete, the calculated results can then be uploaded and displayed in GiD.

3.3.1 Model generation

Modeling in GiD was performed in sequential steps, that are described in greater detail below:

Geometry of the beam: is the first step in modeling. The coordinates of the edges of a cross-section in $[x,y,z]$ are entered to create individual points. These are then connected by lines. Four lines then form a surface, which can be copied to create a volume by extrusion. Reinforcement (bending or shear) is created in the same way – points that describe the position in space are then connected by lines. Supports and loading points were modeled as relatively thin plates and were positioned 0,5 m apart from each other (as in the real experiment described in Chapter 4).

This method of input (i. e. by coordinates) is useful because the geometry of the model can be much more complicated. And by entering individual points one can easily describe any irregularity in the shape or geometry.

The final geometry can be seen on Figure 3.7. Prestressed GFRP reinforcement is the blue line, stirrups are violet and loading and support plates are green. The visibility of concrete itself was switched off, but the shape can be seen by the edges.

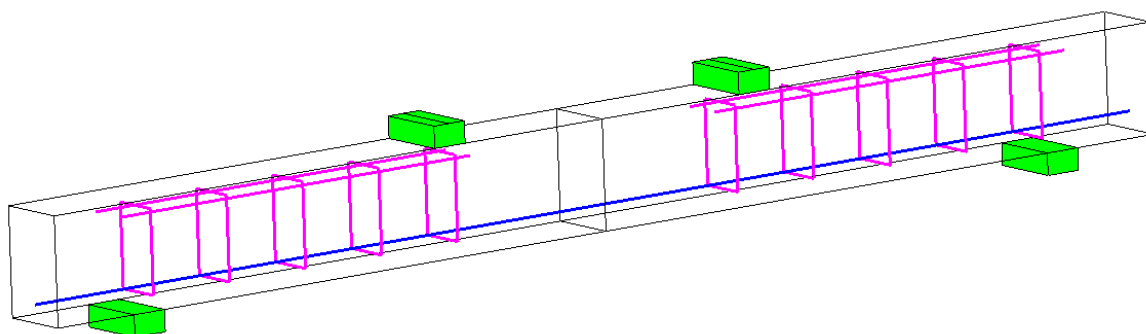


Figure 3.7: Geometry of the model

Material models: are then assigned to the respective volumes. They were based on the calculated mechanical properties of the GFRP rebar (see Chapter 3) and the experimental data from specimens testing (see Chapter 4):

- *Concrete*: 3DNonlinearCementitious2 was used for concrete. It is a fracture plastic model that considers hardening before compressive strength of the material is reached. Incremental formulation is used for the fracturing part of the model [35]. The mechanical properties are calculated from one input value – the mean cubic strength of concrete at the day of testing. The generated values can be later specified as results of specimens testing become available.
- *GFRP*: Reinforcement model was used but its properties had to be modified respectively, i. e. tensile strength was increased, elastic modulus lowered and the stress-strain diagram changed to linear elastic with corresponding parameters. These values were obtained by the micromechanical analysis of a GFRP rebar mentioned in Chapter 3.1.
- *Stirrups*: Reinforcement model was again used but this time left unchanged. It provided a bilinear stress-strain behaviour with respective values for B500A steel, namely different yield and ultimate strengths.
- *Plates*: loading and support. To simulate the experiment described in Chapter 4 into as much detail as possible, loading and support plates had to be included. 3DElasIsotropic was chosen because stresses were not be investigated in these elements. It contained linearly elastic behaviour which was sufficient to simulate real steel supports. It had a significantly higher strength than the rest of the beam.

Loads and supports: were placed on respective plates. Support plates had constrained movement (but both allowed rotation) in order to simulate the real experiment. Load was prescribed as a forced deflection on the upper plates. A total deflection of 40 mm was prescribed but due to the solving method it was divided into a number of steps. The actual number was modified according to the need for exact results. More steps meant that the results were more accurate on the one hand, but on the other hand also increased computing time.

Mesh generation: GiD contains a powerful mesh generator T3D. It allows to generate unstructured, semi-structured or structured mesh. The accuracy of the results and the computational time also depend on the mesh type and size chosen. It is necessary to prescribe the size of the actual element and its type, and the mesh generation is automatic (see Figure 3.8). For six-sided elements it is recommended to use linear elements – *bricks*, but for irregular elements tetrahedra have to be used.

Monitoring points: were chosen and assigned in order to monitor requested values so that they can be compared with experimental results. Force applied on the

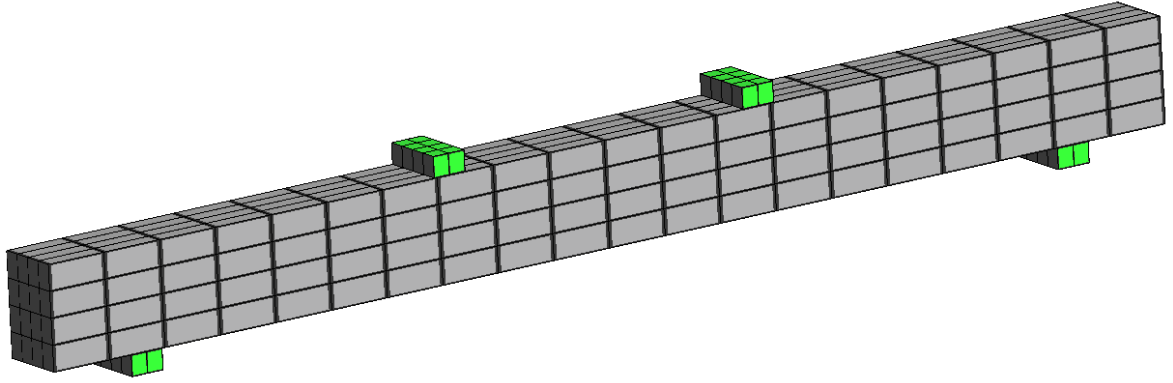


Figure 3.8: Mesh on the model

loading plate and deflection in midspan were monitored because there were the only possible values that could be measured during the experiments. Crack width was also monitored but not confronted with experimental results.

3.3.2 Solution method for numerical analysis

There are two methods in ATENA that can be used to solve nonlinear problems: *Arc-Length* method or *Newton-Raphson* method. Each of these solves the nonlinear system of equations by an iteration process but slightly differently.

Arc-Length method is used to solve unstable problems such as buckling. Spherical iterations and a defined arc length radius are necessary to investigate sharp turns in the force – deflection diagram. The length of the arch can be modified according to the solved problem [36]. Since there are no sharp turns or stability problems expected in my case, this method was not used.

Newton-Raphson method is the default solving method in ATENA software. Similar to *Arc-Length* it is an iterative process based on predictor – corrector scheme that finds the equilibrium between nonlinear equations.

$$K\Delta u = F^a - F^{nr} \quad (3.84)$$

Where: K – stiffness matrix

Δu – displacement vector

F^a – force vector

F^{nr} – vector of restoring loads

Loads are applied in several steps and the balance is calculated in each iteration (see Figure 3.9). It continues until the difference between predictor and corrector is within preset convergence criteria.

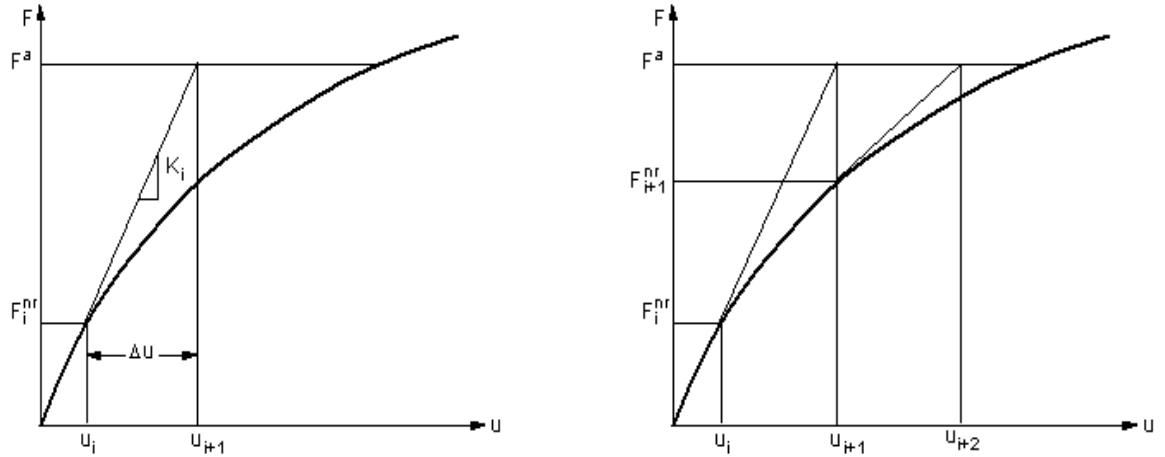


Figure 3.9: Newton-Raphson iteration scheme [36]

3.3.3 Results from numerical analysis

Based on the estimated mean cubic strength (assuming the same concrete mixture used as in [2]), default parameters of the concrete model were generated by ATENA. There were two models to be compared. The *first* contained prestressing as the first loading case. Prestressing was applied as a prescribed initial strain on the reinforcement. Then the model was loaded with prescribed deflection until failure. The *second* model was identical to the first with only one difference – the prestressing was not applied. This was to simulate the effect that the bond between the GFRP reinforcement and concrete was damaged so that the prestressing force was lost. It would behave in the same way as a cross-section reinforced with one GFRP rebar with no prestressing at all. The load bearing capacity before cracking and ultimate capacity were expected to decrease and deflection in midspan to increase as prestressing certainly helps to improve these factors.

During the calculation monitoring points were placed at desired positions, i. e. deflection in midspan and force under loading plates. Force was recalculated into bending moment to make it possible to compare to other specimens that had a slightly different loading scheme (i. e. the forces were not in the thirds of the span, but closer to the middle).

As it can be seen from Figure 3.10, the results are as expected (see Table 3.4). The load bearing capacity of the beam without prestressing before cracking was significantly lowered by 42 % at an approximately same deflection. After cracks appeared, the stiffness of the beam was lowered, hence the bilinear diagram. Ultimate loading capacity decreased by 16 %, but the difference between deflections increased by 88 %.

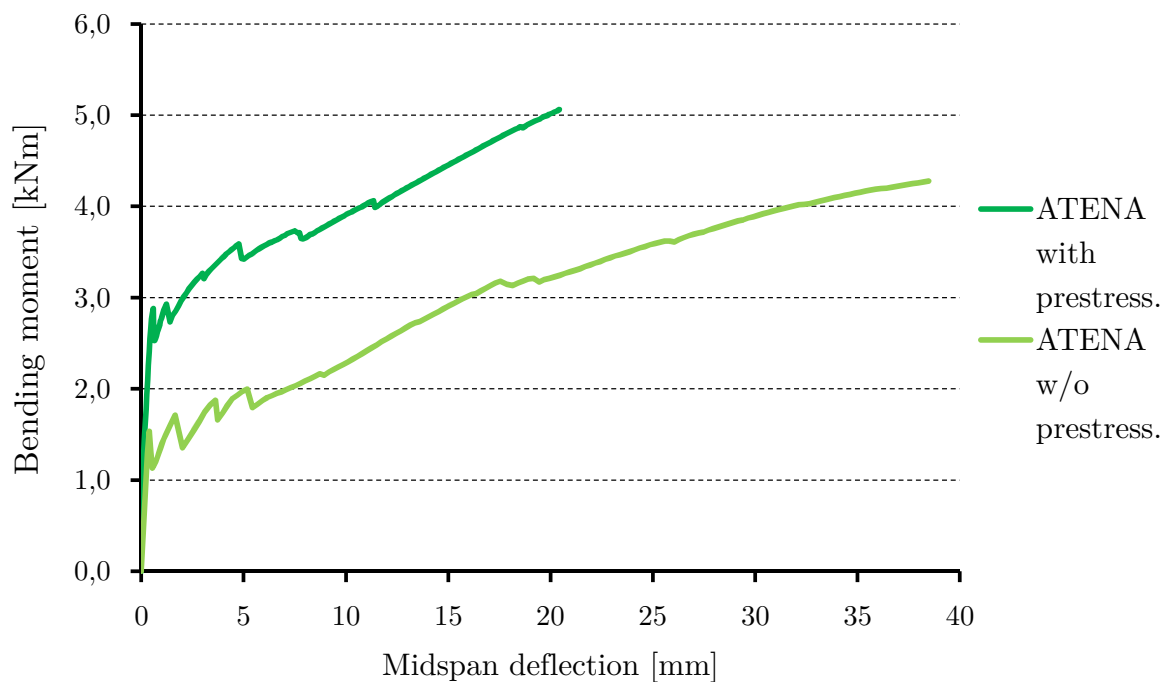


Figure 3.10: Results from ATENA

Table 3.4: Results from ATENA

	Cracking moment [kNm]	Deflection measured [mm]	Ultimate moment [kNm]	Deflection measured [mm]
ATENA with prestressing	2,929	1,223	5,061	20,423
ATENA w/o prestressing	1,710	1,652	4,276	38,467

Chapter 4

Experimental approach

This chapter deals with the experimental part of this thesis. In the following sections the whole experimental procedure is described step by step, starting with the design and production of specimens, their loading and testing followed by a review of the obtained results.

4.1 Design of specimens

Two groups of specimens (see Table 4.1) were produced. Each group contained concrete beams reinforced with prestressed GFRP rebars and support specimens. The proposed beams were 1,8 m long having a cross-section of 100x150 mm. The designed clear span for each beam was 1,5 m so the overlap was 0,15 m on each side of the support. Each beam was prestressed with a composite GFRP rebar. The difference between the two groups was that beams in group 1 contained only a GFRP rebar (without shear reinforcement) and beams in group 2 contained GFRP reinforcement along with steel stirrups (see Figure 4.1).

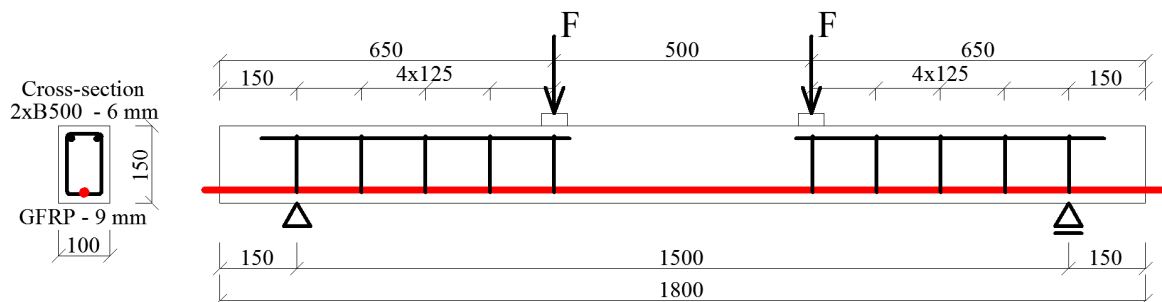


Figure 4.1: Geometry of concrete beams from group 2

Support specimens (see Table 4.1) were also designed and produced for each group in order to determine the properties of concrete and to obtain accurate input characteristics for the ATENA model. Short beams (400 mm long, 100x100 mm cross-section)

were designed to test the tensile strength of concrete in four point bending. Concrete cubes (150 mm) were produced to obtain the compressive characteristics of concrete used, most importantly the compressive strength.

Table 4.1: Overview of specimens

Group	Type	Prestressed GFRP beams		Support specimens	
		No.	shear reinf.	short beams	cubes
1	REF	PGB 1–3	No	GG 7–12	GC 15–18
	F/T	PGB 4–6	No	GG 13–18	GC 11–14
2	F/T	PGB 7–8	Yes	GG 19–24	GC 19–26
	REF	PGB 9–10	Yes	GG 25–30	GC 27–34

The *first group* of samples contained six 1,8 m long beams, twelve 0,4 m long beams (without reinforcement) and eight cubes. One half of these specimens was subjected to thermal loading in a climatic chamber while the other half served as reference specimens. The *second group* of samples contained four 1,8 m long beams, twelve short beams and sixteen cubes. Again one half of specimens served as reference for the other that was subjected to freeze/thaw cycles. Both groups of specimens were cast in several batches due to technological reasons. It was not possible to cast more than three prestressed beams at once due to the lack of manipulation space near the prestressing line for the GFRP reinforcement and given the number of available formwork.

Thermal loading was performed in a climatic chamber. The load bearing capacity of the chamber was restricted to 320 kg (2x80 kg the chamber itself + 200 kg provided by a connecting bridge). Therefore the quantity of specimens placed inside was limited. The weight of the 1,8 m long beams was approximately 68 kg, 0,4 m long beams weighted approximately 10 kg and cubes approximately 8 kg.

4.2 Prestressing composite rebars

GFRP rebars 2,5 m long, 9 mm diameter GFRP were used for the prestressing. They contained anchors at the ends (see Figure 4.2). Anchors were composed of a 25 cm hollow steel tube where the GFRP reinforcement was placed and suffused with expanding cement paste. GFRP consisted of longitudinal alkali-resistant glass fibre strands covered in a thermoset vinyl ester resin. The FVF was 0,58 (and not 0,73 as specified by the manufacturer Prefa Kompozity a.s.). They were one-way spirally wrapped by a flax cord and coated with glued sand to improve bond with concrete (see Figure 4.3). The properties of the reinforcement are summarized in Table 4.2.



Figure 4.2: Anchor at the end of the rebar

Figure 4.3: Close-up on the surface

Clear concrete cover between GFRP rebar and the bottom of the formwork was 20 mm. GFRP rebars do not need a thick concrete cover because of their corrosion resistance. And the thinner the concrete cover, the faster the temperature will reach the rebar, causing it to shrink and expand.

Table 4.2: Reinforcement properties

	Diameter [mm]	Yield strength [MPa]	Ultimate strength [MPa]	Elastic modulus [GPa]	Ultimate strain [%]
GFRP	9	n/a	700	42	1,55
steel B500A	6	500	550	200	$\geq 2,5$

Prestressing was performed in the following steps:

- During the first step, a cage of steel stirrups was positioned on the GFRP rebar. There were 5 stirrups made from 6 mm unfinished tempered carbon steel. Stirrups were held in position with two 6 mm steel bars (see Table 4.2). These did not serve as a structural reinforcement, but only to secure the required distance between individual stirrups.
- The composite rebar was placed in the wooden formwork along with two stirrup cages and positioned in the prestressing line. One anchor was placed in a hollow steel box specially designed for prestressing nonmetallic reinforcement using steel anchors (see Figure 4.4, point “A” and Figure 4.5). The steel box was connected by a threaded steel bar into a HBM load cell (point “B” on Figure 4.4 or Figure 4.6), that allowed us to measure the exact applied prestressing force (see Table 4.3). There was a securing nut (point “C”), that locked the prestressing force once it was applied. Once the rebar was prestressed, the stirrups were tightened to it using a wire.
- Another threaded steel bar was connected to the load cell. This bar was guided through a stabilizing steel structure and ended with a massive nut (point “D”). This nut was continually tightened in order to prestress the GFRP rebar. An

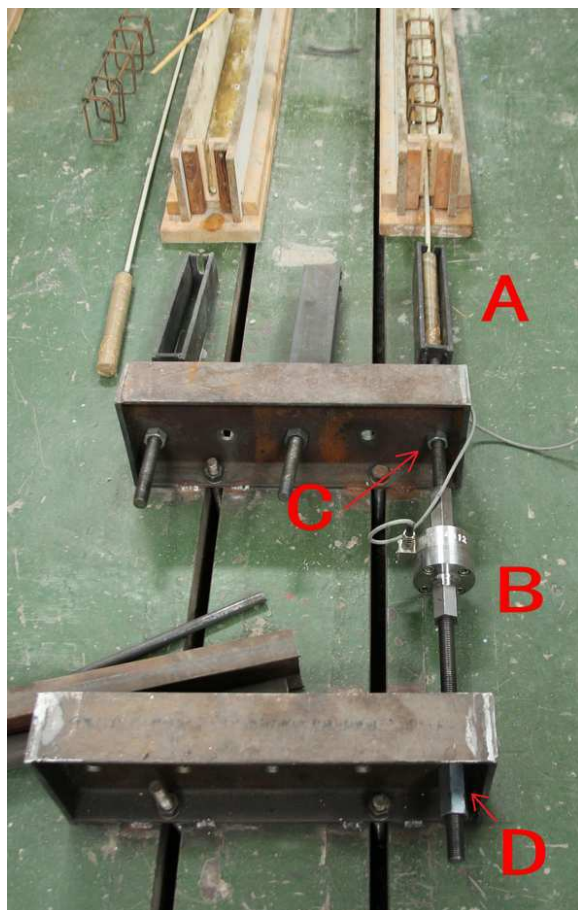


Figure 4.4: Prestressing GFRP rebar



Figure 4.5: Close-up on the anchor



Figure 4.6: Close-up on load cell

exact prestressing force was measured and displayed, so that prestressing could be stopped when the desired force was reached.

- Once the desired force was reached, the securing nut (point “C”) was tightened by hand and the load cell was removed.

4.3 Production of samples

A special mixture of concrete was designed for this application. It was the same mixture as in [2], for specification see Table 4.4. Because freeze/thaw cycles were prescribed for the specimens air-entrained concrete mixture was designed in order to reduce the damage from the changing temperature. A minimal compressive strength of concrete after 28 days was required to be around 30 MPa. Maximum nominal aggregate size used was 8 mm but only because it was necessary in [2], and now it was chosen to extend the database of concrete characteristics.

A series of thermometers were placed inside the beams PGB 7–8 from group 2 to

Table 4.3: Prestressing force

Group	Type	Specimens	Prestressing force [kN]	Approximate elongation [mm]
1	REF	PGB 1	1 350	n/a
	REF	PGB 3	1 350	n/a
1	F/T	PGB 4	1 350	12
	F/T	PGB 5	1 351	13
	F/T	PGB 6	1 354	12
2	F/T	PGB 7	1 380	14
	F/T	PGB 8	1 353	12
2	REF	PGB 9	1 347	13
	REF	PGB 10	1 367	12

Table 4.4: Concrete mixture: components and properties

Components	Quantity or ratio
Aggregate 0–4	850 [kg/m ³]
Aggregate 4–8	800 [kg/m ³]
Cement CEM II/B–S 32,5 R	330 [kg/m ³]
Water	170 [kg/m ³]
Air entraining admixture: SikaAer–200S 0,5%	1,45 [kg/m ³]
Water/cement ratio	0,51 [–]

obtain data necessary to confront it with numerical modeling. To secure their position during concrete casting they were tightened by a wire to the GFRP rebar as well as on the stirrups. There was a total of twelve thermometers used for the beams, six in each (Figures 4.7 and 4.8): two secured to the GFRP rebar in the thirds of the span (T1, T2), one in the middle of the cross-section (T3), two on the outer surface of the beam (T4, T5) and the last one measured the temperature in the climatic chamber (T6).

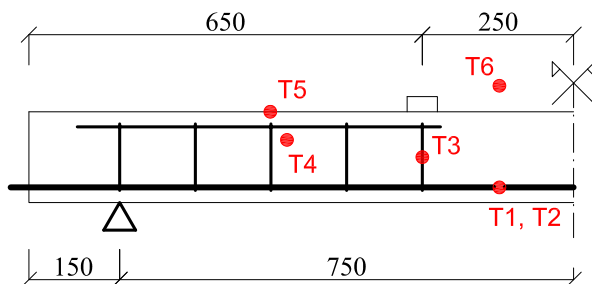


Figure 4.7: Placement of thermometers

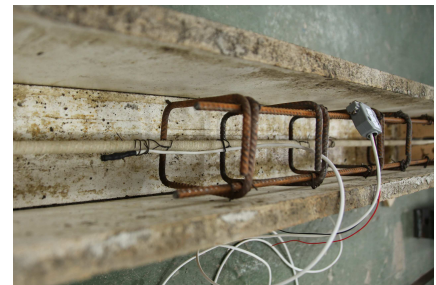


Figure 4.8: Close-up on the thermometer

A thin layer of mineral oil was applied on the inner surface of the formwork (wooden for 1,8 m long beams, steel for 0,4 m beams and plastic for the cubes) in order to reduce friction during demoulding. Concrete was cast in two or three batches depending on the amount of specimens cast. Casting started when all the constituents were placed in a concrete-mixer after weighting. They were mixed for 60 seconds after which the air-entraining admixture was dosed with remaining water. After this step the mixing continued for another 60 seconds for a total time of 2 minutes. Then the cover of the concrete-mixer was lifted, fresh concrete checked and the edges of the container cleaned of unmixed cement. This cleaning was meant to last 60 seconds, 3 minutes total time. Then for the last 60 seconds the fresh concrete was mixed, 30 seconds in one direction and the last 30 seconds in the other direction. After 4 minutes of total time the concrete mixture was ready for casting into the formwork.

The formwork was filled only to mid-height then the mixture was vibrated. Long beams were vibrated using a submersible vibrator. The operator had to vibrate carefully not to touch (and vibrate) the reinforcement. This would cause the aggregate to move away from the reinforcement, lowering bond strength. Short beams and cubes were vibrated on a vibrating table. Then all formwork were filled completely and vibrated again.

Samples were then covered by a plastic foil to reduce water evaporation and watered twice a day. After two days the short beams and cubes were demoulded and cured further in laboratory conditions for a total of 28 days. Long beams were cured also for two days. After 15 days the prestressing force was released into the samples by cutting the reinforcement close to the steel anchor. Samples were then demoulded and kept together with the rest of the specimens.

After 28 days of curing the specimens that were meant to be subjected to freeze/thaw cycles were placed in the climatic chamber. They were kept there for the duration of the prescribed F/T cycle. Samples from *group 1* contained long beams PGB 4–6, short beams GG 13–18 and cubes GC 15–18. These samples were subjected to fifty F/T cycles for 50 days (1 cycle = 24 hours). Samples from *group 2* contained long beams PGB 7–8, short beams GG 19–24 and cubes GC 19–26 and were subjected to fifty F/T cycles for 75 days (1 cycle = 36 hours). The rest of the specimens from the respective groups were kept in laboratory conditions for the duration of the F/T cycles. Afterwards they were tested in the same day as the specimens from the climatic chamber.

4.4 Freeze/thaw cycles

Since design codes do not specify loading with temperature research was conducted in the database of CHMÚ (Czech hydrometeorological institute). The objective was to find the maximal and minimal extreme temperature in Prague in order to simulate realistic temperatures in the climatic chamber. These temperatures were chosen:

- $-30\text{ }^{\circ}\text{C}$ represents the minimal extreme temperature (rounded down). The exact minimal temperature was $-27,6\text{ }^{\circ}\text{C}$ recorded on 1.3.1785.
- $40\text{ }^{\circ}\text{C}$ represents the maximal extreme temperature (rounded up). The exact maximal temperature was $37,8\text{ }^{\circ}\text{C}$ recorded on 27.7.1983.

As it was pointed out in [2] these temperatures are maximal (minimal) extreme air temperatures ever recorded. Average temperatures throughout the year are not even close to them. For example, the average air temperature in Prague throughout the whole year is $10,4\text{ }^{\circ}\text{C}$. The average air temperature during winter is $0,7\text{ }^{\circ}\text{C}$ and during summer $20,1\text{ }^{\circ}\text{C}$. The temperature on a surface of a structure depends also on its colour – the darker, the more it attracts infrared rays and the hotter it gets.

The temperature loading was performed in a CTS climatic chamber C-40/350/s. A change in temperature was programmed as a cycle, that would be repeated. There were two F/T cycles programmed for the specimens. *Group 1* was subjected to the same cycle mentioned in [2] (see Figure 4.9). This cycle started at $20\text{ }^{\circ}\text{C}$ and this temperature was kept constant for a few hours just to equalize the temperature inside the climatic chamber. The temperature cycle started with an increase up to $40\text{ }^{\circ}\text{C}$ in 103 minutes (= 1,72 hours) giving a gradient of $0,2\text{ K/min}$. This is well below the capacity of the chamber itself which can force a temperature gradient of 3 K/min when heating and even 4 K/min when cooling. After reaching $40\text{ }^{\circ}\text{C}$ the temperature was kept constant for 6 hours. Then the interior of the chamber was cooled with the same but negative gradient ($-0,2\text{ K/min}$) for 6 hours, until $-30\text{ }^{\circ}\text{C}$ was achieved. This temperature was kept constant for 6 hours. Afterwards the temperature was increased until $40\text{ }^{\circ}\text{C}$ was achieved (in 6 hours, same temperature gradient). The changes were programmed to occur after 6–6–6–6 hours. This cycle lasted 24 hours, there were fifty cycles programmed and the duration of the loading was 50 days.

Because there were concerns that the temperature change was too quick, the cycle for the specimens from *group 2* was modified. According to the numerical modeling of heat transport in MATLAB (and verified by TRFEL – as explained in Chapter 3), a longer cycle was proposed (see Figure 4.10). This cycle again started at $20\text{ }^{\circ}\text{C}$. The temperature cycle started with an increase up to $40\text{ }^{\circ}\text{C}$ in 51 minutes (= 0,85 hours)

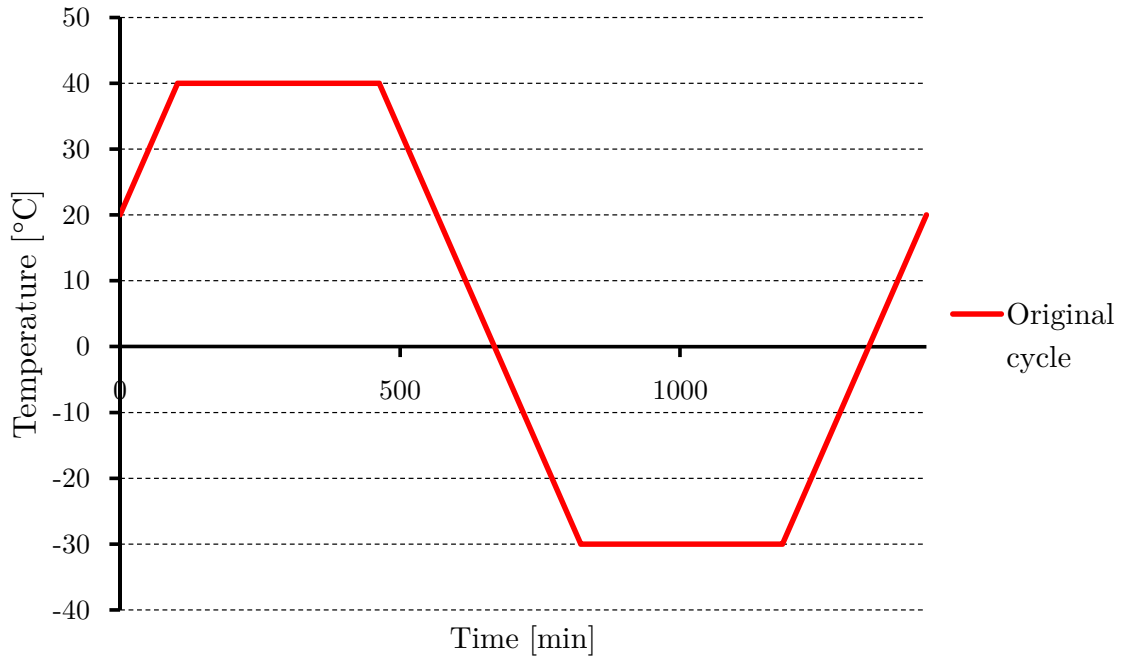


Figure 4.9: Freeze/thaw cycle within 24 hours

giving a gradient of 0,39 K/min. After reaching 40 °C the temperature was kept constant for 15 hours. Then the interior of the chamber was cooled with a gradient $-0,39$ K/min during 3 hours until -30 °C was achieved. This temperature was kept constant for 15 hours. Afterwards the temperature was increased until 40 °C was achieved (in 3 hours using same temperature gradient). The changes were programmed to occur after 15–3–15–3 hours. This cycle lasted 36 hours and there were fifty cycles programmed. The whole temperature loading lasted 75 days.

An overview of used freeze/thaw cycles can be found in Table 4.5.

Table 4.5: Overview of freeze/thaw cycles

Cycle	Constant temp. 40 °C for [hours]	Δ /time [K/min /hours]	Constant temp. –30 °C for [hours]	Δ /time [K/min /hours]
Original	6	-0,2 / 6	6	0,2 / 6
Modified	15	-0,39 / 3	15	0,39 / 15

After the temperature loading the specimens were then subjected to destructive testing as it is described in the following chapter.

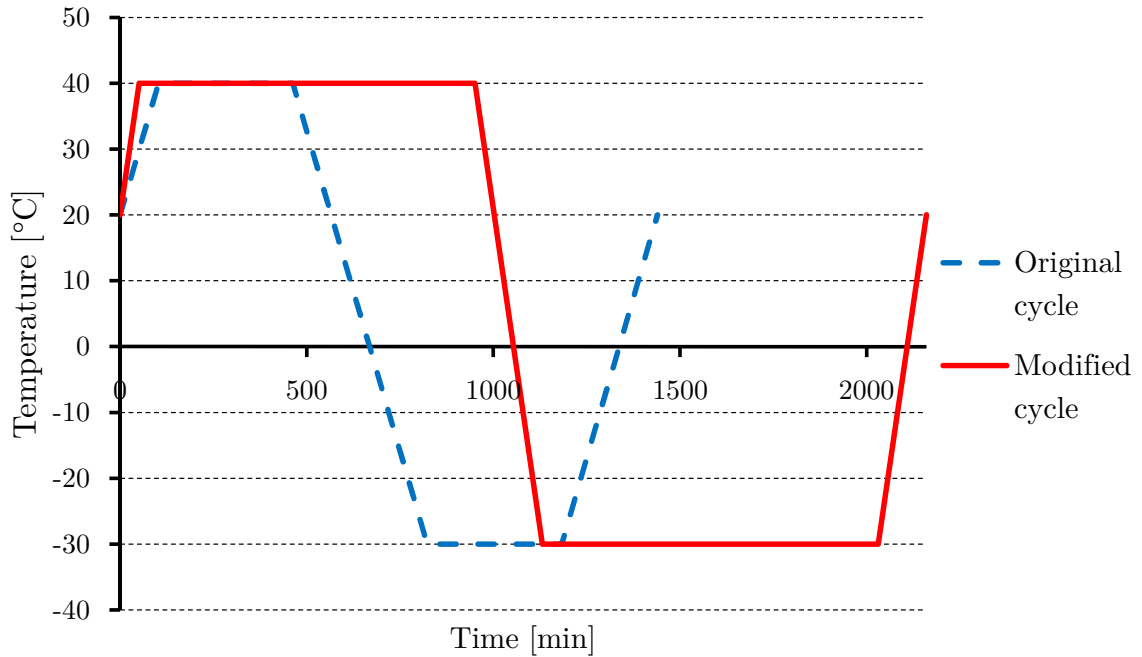


Figure 4.10: Freeze/thaw cycle within 36 hours

4.5 Testing of specimens

Various parameters were tested during concrete production and on final specimens to determine the required characteristics for the ATENA model.

4.5.1 Determination of air content

It was necessary to verify the amount of entrained air in fresh concrete. The air entraining admixture created closed air bubbles of a prescribed diameter. Should the water in concrete freeze and expand, it would do inside these bubbles. The integrity of the specimens is not damaged making concrete more durable and resistant to freeze/thaw cycles.

Measuring of actual air volume on fresh concrete is needed to verify the precise dosing of the admixture. There are very strict limit values for the volume of entrained air: a minimal value is approx. 5 %, while the maximal value is 9 %. If the air content is lower than 5 %, there may not be enough bubbles to improve the durability of concrete. If the air content is higher than 9 %, the mechanical parameters of concrete deteriorate drastically, making the concrete useless.

While there are more methods to determine the air content, *pressure method* was used. It is based on observation of the change in volume of concrete with a change of

pressure. A special device called air meter (see Figure 4.11) is necessary. It consists of two parts – a stainless steel bowl and a cover assembly containing a dial. The principle of this method is in leveling a known volume of air at a known pressure in a sealed air chamber with the unknown volume of air in concrete [2]. Approximate value of the air content is then displayed on a dial. Concrete inside the bowl can not be then reused for specimens after the testing as it is saturated with water.



Figure 4.11: Air meter showing approximate air content

The air content was measured three times for each batch. The first measure was on a testing mixture of 20 litres of concrete. It manufactured only to verify and optimize the amount of air entraining admixture needed. Regardless of the result this concrete batch was discarded afterwards. Measured results are presented in Table 4.6.

As it can be seen from the results, the dosing of the air entraining admixture greatly influences the amount of entrapped air. Huge effort was made to measure the amount as precise as it could be done but the dosage of other constituents also influenced the final result. The volume of air lies in acceptable values which should improve the durability of concrete subjected to freeze/thaw cycles.

Table 4.6: Measured air content

Group	Specimens and support samples	Type	Average % of entrained air
1	PGB 1–3	REF	7,0
	PGB 4–6	F/T	5,2
2	PGB 7–8	F/T	5,0
	PGB 9–10	REF	5,5

4.5.2 Verification of temperature

Temperature was measured during freeze/thaw cycling. Thermometers were installed in the beams themselves (PGB 7–8), on their surface and in the climatic chamber itself. Thermometers inside the beams were used to verify the numerical model of non-stationary heat transport presented in Chapter 3. Temperature was measured in three places: in the middle of the concrete cross-section, in the GFRP prestressed rebar and on the surface of the beam. The placement of thermometers can be seen on Figure 4.7 and in Table 4.7. Thermometers T6 and T12 were used to measure the temperature inside of the climatic chamber to verify the prescribed temperature.

Table 4.7: Placement of thermometers in beams PGB 7–8

Specimens	GFRP rebar (thirds of span)	Middle of the concrete cross-section	Outer surface
PGB 7	T1, T2	T3	T4, T5
PGB 8	T7, T8	T9	T10, T11

Temperature measured on the GFRP rebar, in the middle of the cross-section and on the outer surface of the concrete beams was then confronted with the numerical model and the comparison can be seen on Figures 4.12, 4.13 and 4.14 respectively. Both temperature measurements were confronted with their respective temperature predictions from the numerical model.

The results show a great compliance with the numerical model. The model was constructed so that it could be easily modified on different (but rectangular) cross-sections, the mesh size could be changed easily as well as the length of the freeze/thaw cycle. But the input constants still influence the calculation. By using those mentioned in Table 3.3 and the same concrete mixture presented in Table 4.4, this model can be used with great success to estimate the layout of temperature field over a desired rectangular cross-section with a desired temperature cycle.

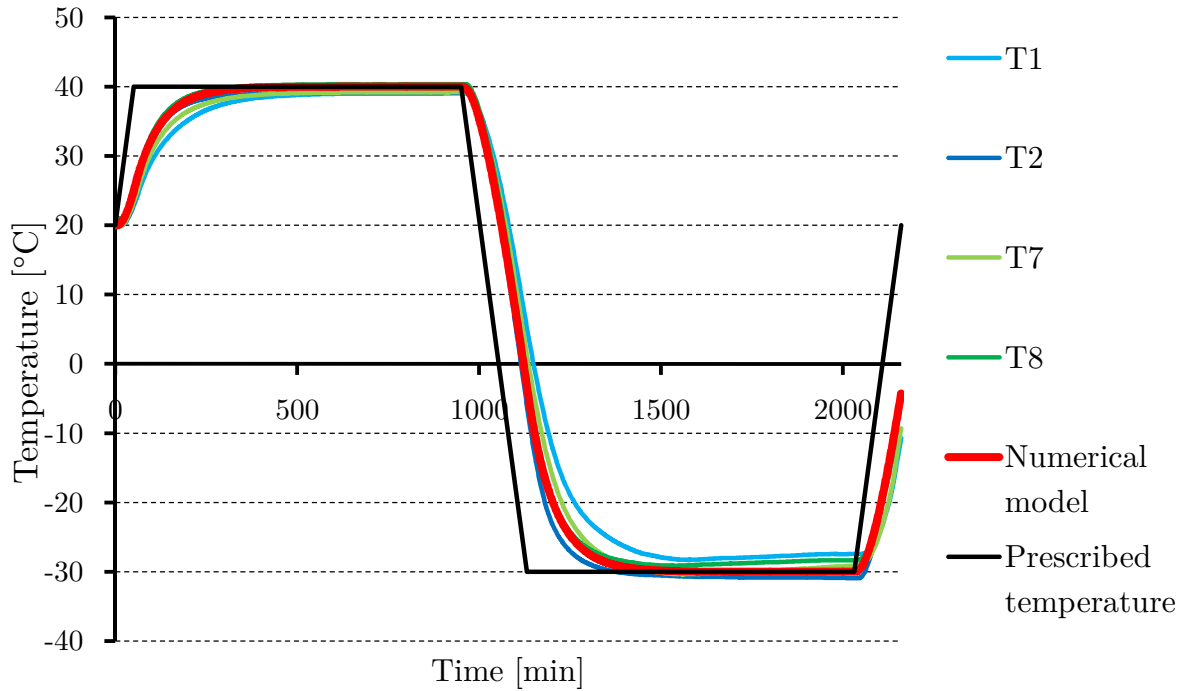


Figure 4.12: Measured temperature on the GFRP rebar

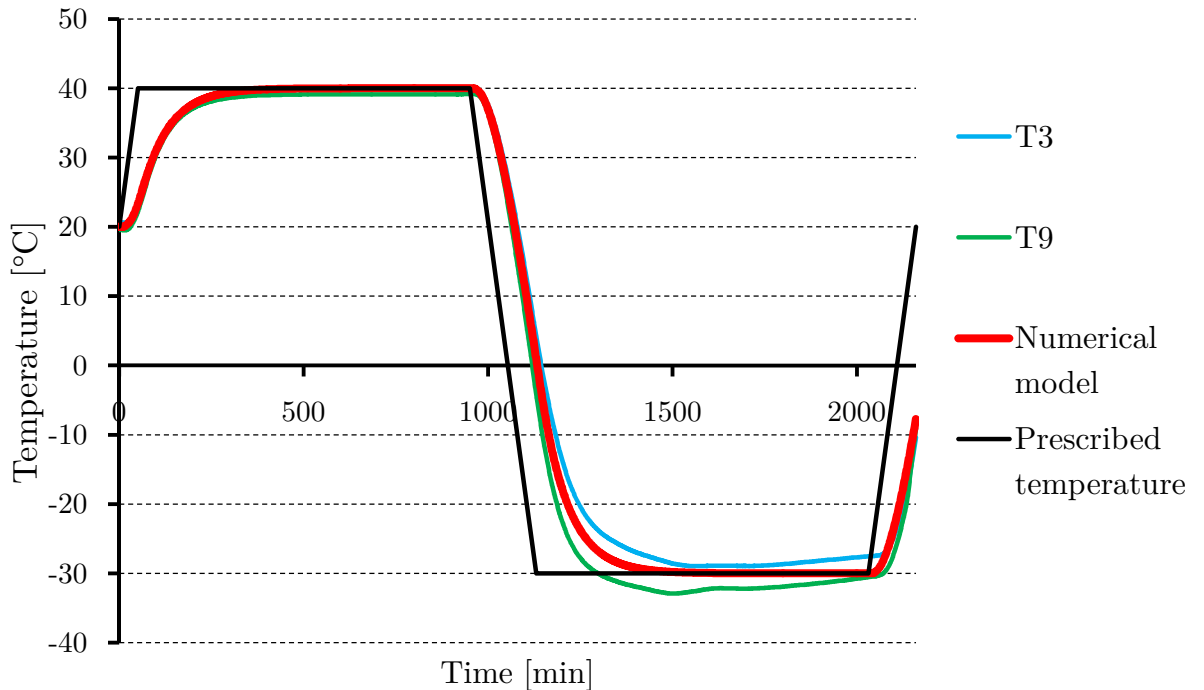


Figure 4.13: Measured temperature in the middle of the cross-section

4.5.3 Compressive strength of concrete

Compressive strength of concrete was measured according to [37] on all cubes. Prior to the testing the dimensions of all cubes were taken along with their weight. Samples

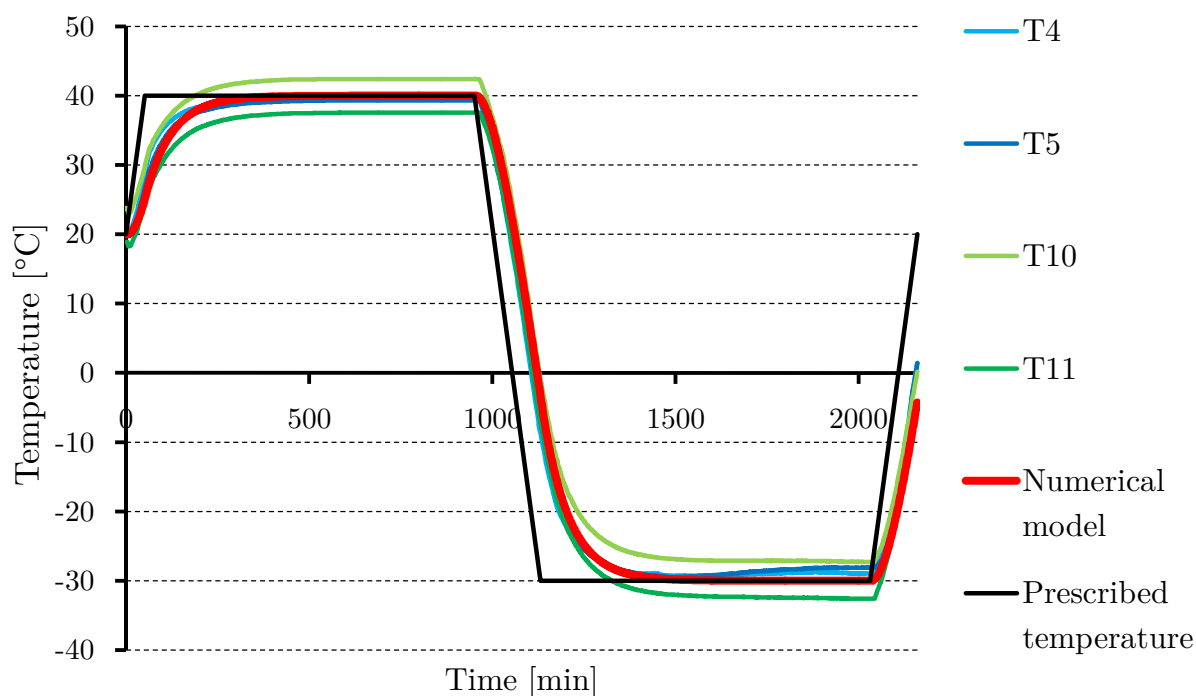


Figure 4.14: Measured temperature on the outer surface

were then placed one-by-one in a loading machine in the direction perpendicular to the vibration (see Figure 4.15).



Figure 4.15: Test setup (left) and prescribed way of destruction of the sample (right)

Compressive strength of concrete cubes from *group 1* is presented in Tables 4.8 (subjected to F/T) and 4.9 (reference). Results of samples from *group 2* are in Tables 4.10 (subjected to F/T) and 4.11 (reference). Average values of density and compressive strength for all specimens are then compared in Table 4.12.

As it can be seen from the results, compressive strength of specimens exposed to freeze/thaw cycling in a climatic chamber was not deteriorated. The values vary by

Table 4.8: Compressive strength of samples from group 1 subjected to F/T cycles

Specimens	Weight [kg]	Density [kg/m ³]	Force [kN]	Compressive strength [MPa]
GC 11	7,660	2 238	940	41
GC 12	7,496	2 199	963	42
GC 13	7,543	2 208	862	38
GC 14	7,379	2 201	991	44
Mean value		2 210		41
St. deviation		18		3

Table 4.9: Compressive strength of reference samples from group 1

Specimens	Weight [kg]	Density [kg/m ³]	Force [kN]	Compressive strength [MPa]
GC 15	7,317	2 177	930	41
GC 16	7,611	2 236	1 041	46
GC 17	7,604	2 244	1 005	44
GC 18	7,695	2 256	1 085	48
Mean value		2 230		45
St. deviation		35		3

Table 4.10: Compressive strength of samples from group 2 subjected to F/T cycles

Specimens	Weight [kg]	Density [kg/m ³]	Force [kN]	Compressive strength [MPa]
GC 19	7,173	2 137	812	36
GC 20	7,319	2 164	779	35
GC 21	7,434	2 164	815	36
GC 22	7,364	2 178	860	38
GC 23	7,292	2 134	850	37
GC 24	7,318	2 163	845	37
GC 25	7,121	2 177	795	36
GC 26	7,341	2 199	895	40
Mean value		2 164		37
St. deviation		21		2

small amounts and lie within standard deviations due to the fact that air entraining admixture was used. It can also be observed that regardless of the length of temperature loading the specimens retained their mechanical properties as once the loading lasted 50 days and then 75 days of extreme temperature changes. It can be therefore stated that the admixture was chosen correctly, performed as it was designed and ex-

Table 4.11: Compressive strength of reference samples from group 2

Specimens	Weight [kg]	Density [kg/m ³]	Force [kN]	Compressive strength [MPa]
GC 27	7,444	2 194	850	38
GC 28	7,401	2 184	790	35
GC 29	7,498	2 192	880	39
GC 30	7,564	2 186	900	39
GC 31	7,411	2 187	907	40
GC 32	7,342	2 203	860	39
GC 33	7,298	2 165	841	37
GC 34	7,401	2 180	855	38
Mean value		2 186		38
St. deviation		11		2

Table 4.12: Overview of the mean values for all specimens

Group	Type	Specimens	Density [kg/m ³]	Compressive strength [MPa]
1	F/T	GC 11–14	2 210 ± 18	41 ± 3
	REF	GC 15–18	2 230 ± 35	45 ± 3
2	F/T	GC 19–26	2 164 ± 21	37 ± 2
	REF	GC 27–34	2 186 ± 11	38 ± 2

pected. This enabled us to compare results from a numerical simulation in ATENA without having to modify the material model since freeze/thaw cycles did not affect the mechanical properties of concrete.

4.5.4 Tensile strength of concrete

Tensile strength was investigated only to correct the default value calculated by ATENA software. Every material parameter in ATENA is calculated only from the average value of cubic strength. It is valid for a “average” concrete mixture. Since our mixture contained maximum aggregate 4–8 and entrained air the default material model generated by ATENA had to be modified.

Tensile strength in bending was investigated on short beams (0,4 m long, 0,1x0,1 m cross-section). The beam was placed on steel cylindrical supports with a clear span of 300 mm. One loading plate (containing cylinders) was positioned in thirds of the span, atop the beam, 100 mm apart, 150 mm from the edge, as seen on Figure 4.16.



Figure 4.16: Test setup (left) and prescribed way of destruction of the sample (right)

The beams were loaded by a hydraulic press and the maximal force was measured. It was then recalculated into tensile strength – elastic redistribution of strain was considered and the maximal stress on the lower side of the cross-section was considered the tensile strength. The results from *group 1* are presented in Tables 4.13 (reference) and 4.14 (subjected to F/T). Results of samples from *group 2* are in Tables 4.10 (subjected to F/T) and 4.11 (reference). Average values of tensile strength for all specimens are then compared in Table 4.17.

Table 4.13: Tensile strength of reference samples from group 1

Specimens	Measured force [kN]	Tensile strength [MPa]
GG 7	17,8	5,3
GG 8	17,1	5,1
GG 9	14,4	4,3
GG 10	14,6	4,4
GG 11	19,0	5,7
GG 12	17,6	5,3
Mean value		5,0
St. deviation		0,6

Results show a slight deterioration of tensile strength for the first group of samples. This can be attributed to the manufacturing process as casting of concrete was not performed with the highest possible quality (traces of not-excellent quality could be observed on all specimens from that group, not only short beams). The same aspect can be observed when comparing results of the compressive strength. The results show that by using air entraining admixture the mechanical properties of concrete were not severely deteriorated but a slight lowering can be observed regardless of time of exposure to the freeze/thaw cycle.

Table 4.14: Tensile strength of samples from group 1 subjected to F/T cycles

Specimens	Measured force [kN]	Tensile strength [MPa]
GG 13	15,3	4,6
GG 14	15,3	3,9
GG 15	13,6	4,2
GG 15	12,7	3,8
GG 17	14,3	4,3
GG 18	13,2	3,9
Mean value		4,1
St. deviation		0,3

Table 4.15: Tensile strength of samples from group 2 subjected to F/T cycles

Specimens	Measured force [kN]	Tensile strength [MPa]
GG 13	15,0	4,6
GG 14	14,9	4,4
GG 15	12,9	3,8
GG 15	17,1	5,0
GG 17	13,5	4,1
GG 18	15,8	4,7
Mean value		4,4
St. deviation		0,4

Table 4.16: Tensile strength of reference samples from group 2

Specimens	Measured force [kN]	Tensile strength [MPa]
GG 13	18,8	5,5
GG 14	13,3	3,8
GG 15	18,0	5,2
GG 15	14,6	4,3
GG 17	15,0	4,4
GG 18	17,3	5,1
Mean value		4,7
St. deviation		0,6

4.5.5 Four–point bending test

A four-point bending test was performed on each beam (for scheme see Figure 4.1) to obtain the maximum load bearing capacity. The beam was placed on steel cylin-

Table 4.17: Overview of the mean values of tensile strength

Group	Type	Specimens	Tensile strength [MPa]
1	REF	GG 7–12	$5,0 \pm 0,6$
	F/T	GG 13–18	$4,1 \pm 0,3$
2	F/T	GG 19–24	$4,4 \pm 0,4$
	REF	GG 25–30	$4,7 \pm 0,6$

drical supports with a clear span of 1500 mm. Two loading plates were positioned in thirds of the span, atop the beam, 500 mm apart, 650 mm from the edge. Two standard deflection gauges were fitted in the middle of the span on the beam to measure deflection. The average deflection was calculated afterwards as a mean value. The load was applied by a hydraulic press EU 40 and was distributed evenly on the loading plates by a steel traverse (see Figure 4.17).



Figure 4.17: Test configuration of concrete beams

Beams were loaded by a prescribed force in 0,02 kN/sec increments. The time was not checked because the experiments were stopped when the beam reached its load bearing capacity and collapsed. The maximal force generated by the press was recorded along with the deflection in midspan. The force was then recalculated into a bending moment (which was constant in the middle of the beam due to the configuration of loading forces and support). An average value of deflection was also calculated and recorded.

The moment – deflection diagram shows bilinear behaviour. Beams behaved in a linear elastic way until cracking moment was reached. Then stress on the lower side of the cross-section overcame the tensile strength of concrete and first cracks were opened. Cracks on both group of beams were caused by bending as they were perpendicular to the axis of the beam and in periodical distances from each other. Stiffness of the beam was reduced as the loading continued and cracks began to propagate. Loading continued until the load bearing capacity was reached and the beams collapsed. The mode of collapse varied for each group. But both groups failed by approximately the same loading force so the mode of collapse was only informational.

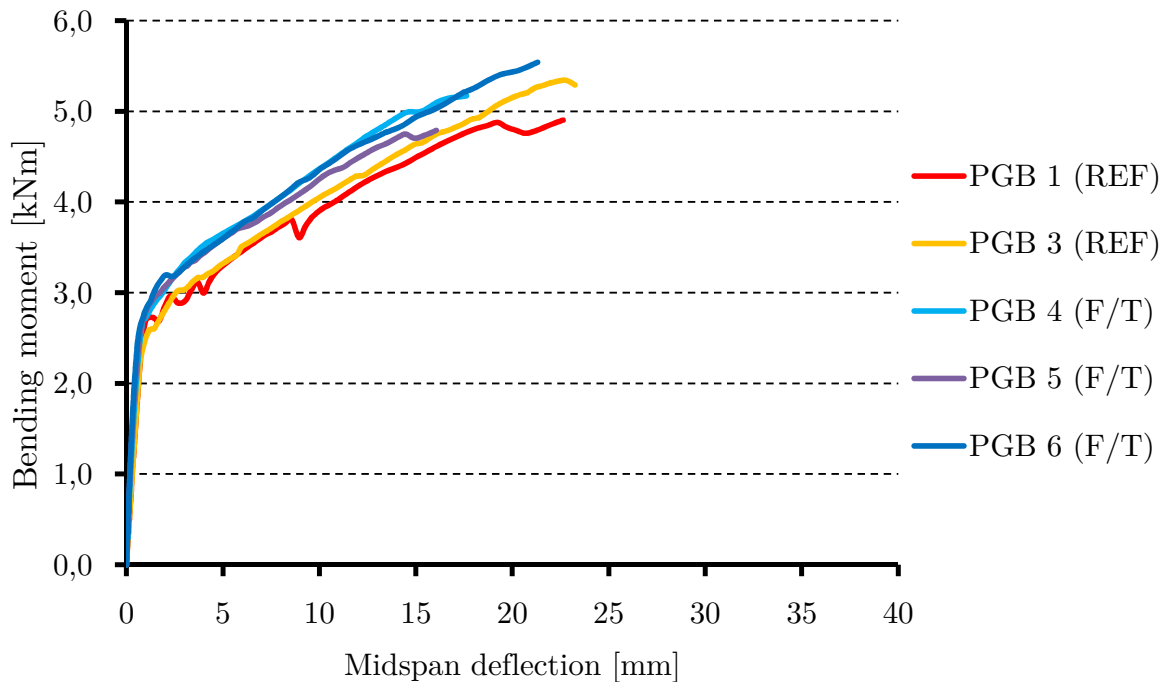


Figure 4.18: Results of beams from group 1

The mode of collapse was predicted by the numerical model in ATENA. It suggested that all beams would collapse by bending regardless whether they contained shear reinforcement or not. Due to this reason the first group of beams were produced without shear reinforcement. But unfortunately the shear capacity and the bending capacity were extremely close to each other so the beams without shear reinforcement failed by shear (as seen of Figure 4.20). But the ultimate measured force corresponded very well with the prediction from the ATENA model (which contained no shear reinforcement and the beam collapsed nonetheless by bending). Since the beams were expected to collapse by bending new beams (from group 2) were cast containing shear reinforcement. These were subjected to the same four point bending test and failed by crushing of concrete due to bending (see Figure 4.21).

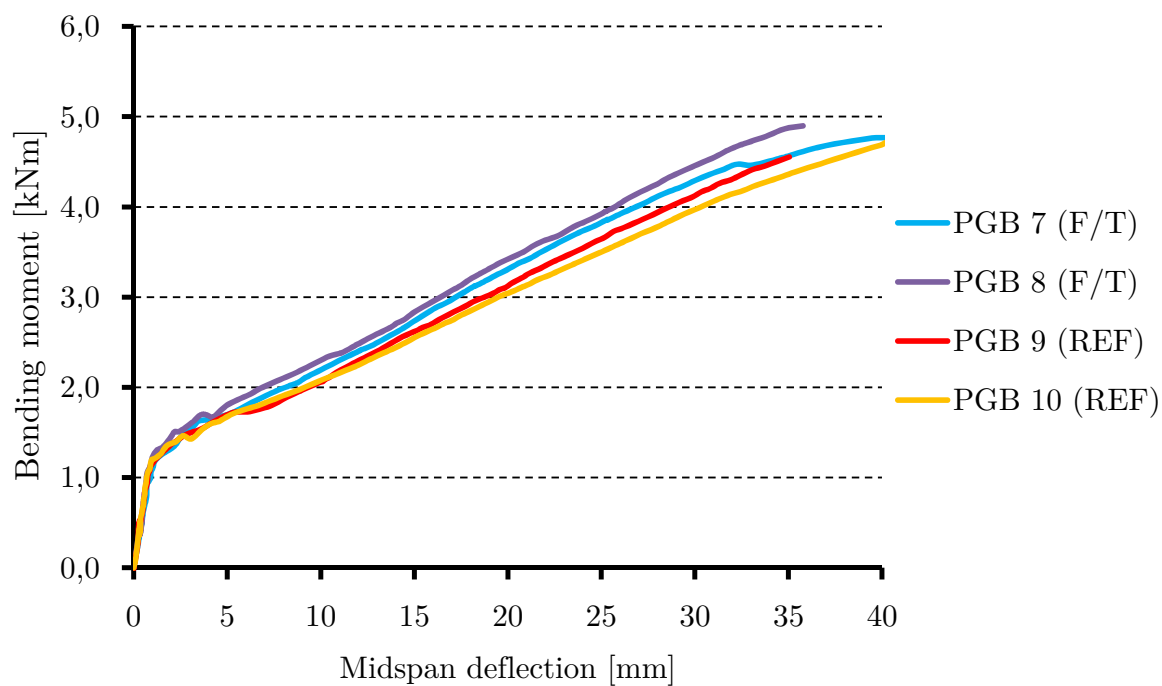


Figure 4.19: Results of beams from group 2

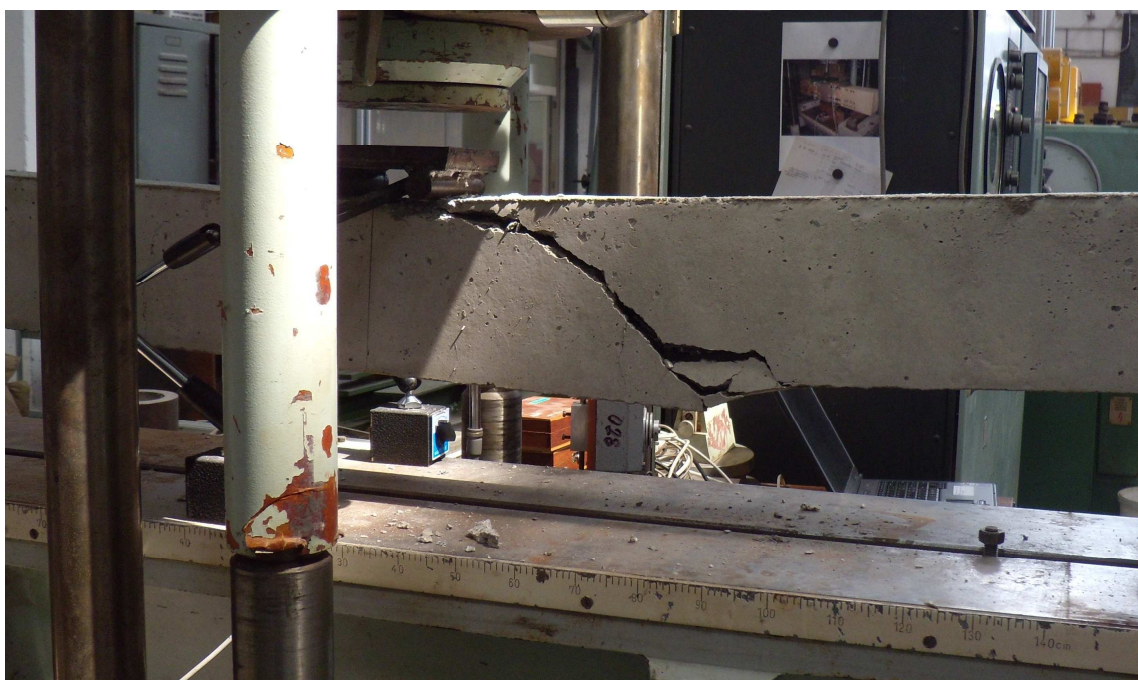


Figure 4.20: Collapsed beam by shear from group 1

Regardless of the mode of failure, by comparing specimens in each group it can be stated that freeze/thaw cycles do not affect the load bearing capacity of the beams. All specimens in one group behaved very similarly – their cracking moment along with



Figure 4.21: Collapsed beam by bending from group 2

its corresponding deflection was very similar, as was the ultimate load bearing capacity. Measured results from experiments along with results from numerical modeling in ATENA are presented in Table 4.18.

What draws attention however is the difference of cracking moments for each group (see Figure 4.22). Cracking moment for the first group was approximately 3 kNm but for the second group it was reduced by approximately 50 %. This would suggest that the modified (longer) freeze/thaw cycle damaged the bond between the GFRP rebar and concrete and the prestressing force was dissipated. Beams from group 2 behaved exactly as the numerical model in ATENA (without prestressing) predicted.

Table 4.18: Load bearing capacity of prestressed GFRP beams

Group	Type	Specimens	Mode of failure	Bending moment [kNm]	Average deflection [mm]
1	REF	PGB 1	Shear	4,905	22,632
	REF	PGB 3	Shear	5,342	22,787
1	F/T	PGB 4	Shear	5,171	17,624
	F/T	PGB 5	Shear	4,791	16,064
	F/T	PGB 6	Shear	5,540	21,318
2	F/T	PGB 7	Flexural	4,768	40,163
	F/T	PGB 8	Flexural	4,897	35,780
2	REF	PGB 9	Flexural	4,553	35,048
	REF	PGB 10	Flexural	4,730	40,784
ATENA	with prestres.		Flexural	5,061	20,423
	w/o prestres.		Flexural	4,276	38,467

Note: PGB 2 from group 1 was discarded from testing due to its overall poor condition after demoulding.

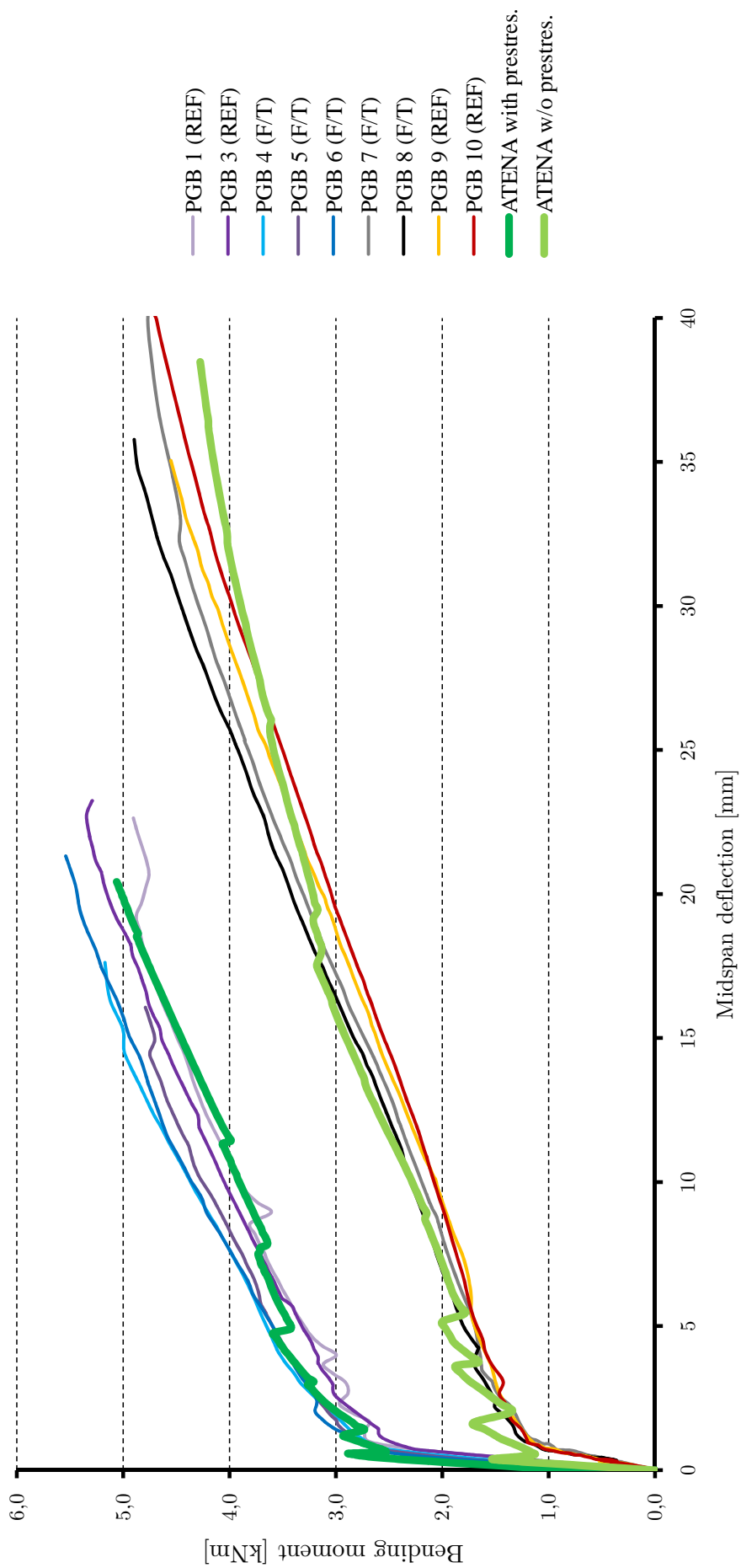


Figure 4.22: Results of all beams

Chapter 5

Conclusion and further research

Several interesting fact were discovered and are summarized for a better outlook in the next sections.

5.1 Resume from numerical modeling

5.1.1 Micromechanical analysis of a lamina

Three methods sorted by their complexity were presented in order to estimate the mechanical properties of the GFRP rebar. This procedure was necessary because its manufacturer (Prefa Kompozity, a. s.) did not provide any additional information about them apart from only an *estimate* of the ultimate strength of the rebar (> 650 MPa). They also provided the FVF (fibre volume fraction) that is an essential indicator for all composite materials. Prefa Kompozity stated that their rebars had an $FVF = 0,73$ (i. e. the amount of fibres in the composite is 73 % by volume). The amount of fibres is restricted by the manufacturing process. GFRP rebars were made by pultrusion process. And products made by this process usually have an FVF from 0,43 to 0,83 [5].

I used mechanical properties of glass fibres (obtained from the manufacturer Saint-Gobain Vetrotex) and vinyl ester matrix along with the suggested $FVF = 0,73$ to estimate the resultant mechanical properties of the composite rebar. I used three methods (Strength of material approach, Halpin–Tsai approach and homogenization by Mori–Tanaka) and found that the properties do not match those experimentally tested.

The elastic modulus of the rebars was measured by nanoindentation and also by testing of the ultimate tensile strength (stress-strain diagram for GFRP composite is linear elastic until failure so the elastic modulus can be obtained from this test). Results from these methods suggested that the elastic modulus varies around 43 GPa.

This modulus depends mostly on the elastic modulus of the glass fibres (which can be considered constant as it does not change from one manufacturer to another) and the FVF. By modifying FVF I found that to get the presumed (and anticipated) elastic modulus, the FVF had to be lowered from 0,73 to 0,58. By increasing the volumetric amount of the vinyl ester resin (which is definitely cheaper than glass fibres) this makes the production cheaper for the manufacturer. Or it can show that the manufacturing process could be improved to obtain rebars with improved mechanical properties.

5.1.2 Modeling of heat transport

Modeling was performed to verify and optimize the temperature cycle so that the extreme temperatures (40 °C and -30 °C) would affect the rebar causing it to shrink and expand. This would damage the bond strength and affect prestressing force. Several cycles were tested and the most effective was chosen. Its duration was 36 hours and fifty freeze/thaw cycles were performed on specimens from group 2. The whole temperature loading lasted 75 days.

My model was written in MATLAB code but to verify its functionality another model in a different had to be used. TRFEL was chosen as it enabled me to use prescribed transfer of flux – a boundary condition that described the environment in the climatic chamber in the most realistic way. Both models used identical input consisting of material parameters, cross-section dimensions and mesh type and size. Both models then provided accurate results of temperature development in time when confronted with experimental data.

5.1.3 Nonlinear analysis in ATENA

A 3D model was made in ATENA to predict the behaviour of prestressed concrete beams with GFRP reinforcement. Input parameters for the material model of concrete were obtained from experiments described in Chapter 4. Material model for GFRP reinforcement was modified according to the results obtained in Chapter 3. The model was loaded once with prestressing force applied and a second time without the prestressing force. Results very precisely predicted the behaviour of experimental testing of beams along with their ultimate load bearing capacity and deflection in midspan.

5.2 Resume from experimental approach

Mechanical properties of concrete were not deteriorated by any of the freeze/thaw cycles applied. The same amount of air entraining admixture was used in both mixtures and results of compressive and tensile strength testing indicate that there is only

a minor change in the absolute mean values of the respective strengths. It can be therefore stated that by the use of this admixture the concrete specimens withstood the climatic loading almost unchanged and that it was not necessary to modify the material model for concrete in ATENA.

The cracking moment of beams subjected to a four point bending test depended on the quality of concrete, rebar and prestressing force inside. The quality of concrete was judged from the testing of mechanical properties (compressive and tensile strength in four point bending) and the results show that freeze/thaw cycles did not deteriorate the mechanical properties. Rebars used for each beam were from the same material so their mechanical properties should be very similar (not identical due to the fact that they were manufactured as a composite material). If the rebar shrank and expanded due to the freeze/thaw cycles it would damage the bond with concrete and the prestressing force would be lower. This behaviour was observed on the numerical model from ATENA. Cracking moment was different for beams from both groups. It strongly depended on the prestressing force as the cracking moment was lowered by almost 50 % when prestressing was excluded.

Beams from group 1 performed as if they did not lose the prestressing force at all. They were subjected to the original freeze/thaw cycle which lasted only 50 days. But regardless of the temperature loading all beams including reference beams performed in the same way. Their load bearing capacity did not change at all and they behaved as the model in ATENA with the prestressing force applied.

On the other hand all beams from group 2 performed as if their prestressing was lost. This result would be acceptable and according to the expectations if only beams subjected to freeze/thaw cycles behaved in this way. Their loading with temperature was longer (it lasted 75 days compared to only 50 days from beams from group 1). But reference beams behaved as if their prestressing force was lost also. But for this effect there were no reasons and they should behave in the same way as all beams in group 1.

The reasons remain unclear as why the reference beams behaved as if they lost all prestressed force. The force was applied in the same way as for beams in group 1. Same methodology was used, same sequence and same tools. The force was checked by the elongation on the rebar (approximately of course) and on computer connected to a load cell (for precise measurement). When the prestressing was applied (i. e. 15 days after casting), the formwork “moved” as the force was applied. Curing was the same but the age of the specimens from group 2 at the day of testing was slightly different due to the longer temperature loading when compared to specimens from group 1. The

only difference was that beams from group 2 contained shear reinforcement. But this fact hardly influenced the prestressing force.

This fact raised more questions than answers, but nonetheless it can be stated that freeze/thaw cycles do not decrease the ultimate loading capacity of beams. GFRP rebars can be safely used for prestressing as this fact dramatically lowers the deflections in midspan (by almost 50 %) and the load bearing capacity remains the same. The disadvantage of GFRP rebars (compared to steel), its low elastic modulus can be suppressed. More beams would be necessary to fully answer the raised question. But due to the enormous time demand it was not possible to fabricate additional prestressed beams to verify the cracking moment.

5.3 Suggestions for further research

Reference beams from group 2 behaved as if they lost all the prestressing force. Why this happened remains unclear. The experiment was very time demanding as it took at least 103 days (28 of curing and 75 day during which part of the samples were loaded with freeze/thaw cycles). It would be definitely interesting to produce another series of prestressed GFRP beams to rule out the possibility that prestressing force dissipated by cracks due to rough handling during demoulding (which is unlikely to happen as the prestressing force makes the beam stiffer) or by relaxation of the GFRP rebar itself (a possible explanation). One way to investigate it would be to use strain gauges on different places on the rebar itself to obtain the force that is applied (right after prestressing and before testing).

Bibliography

- [1] Procházka, J. *Navrhování betonových konstrukcí 1*. ČBS Servis, s. r. o., 3rd edition, (2007).
- [2] Hlobil, M. *Bond properties of GFRP reinforcement in concrete after freeze/thaw cycles*. Czech Technical University in Prague, (2010).
- [3] Eurocode EN 1992-1-1. *Design of concrete structures – General rules and rules for buildings*. CEN – European committee for standardization, (2004).
- [4] ČHMÚ. viewed 28.9.2011 on <http://portal.chmi.cz/>.
- [5] Cabrnoc, B. *Kompozitní materiály a jejich vlastnosti*. Letní škola kompozitních materiálů a konstrukcí, (2011).
- [6] Ehrenstein, G. *Polymerní kompozitní materiály*. Nakladatelství SCIENTIA, s. r. o., (2009).
- [7] Hoa, S. *Principles of the manufacturing of composite materials*. DEStech Publications, Inc., (2009).
- [8] Pompe, V. *Příklady z praxe s kompozitními materiály*. Letní škola kompozitních materiálů a konstrukcí, (2011).
- [9] Barbero, E. *Introduction to composite materials design*. CRC Press, Taylor and Francis Group, 2nd edition, (2011).
- [10] Technical report by fib. *FRP reinforcement in RC structures*. Number 40. International Federation for Structural Concrete, (2007).
- [11] viewed 16.10.2011 on <http://www.owenscorning.com/composites>.
- [12] Kaw, A. *Mechanics of composite materials*. CRC Press, Taylor and Francis Group, 2nd edition, (2006).
- [13] Toray. viewed 17.10.2011 on <http://www.toraycfa.com/product.html>.
- [14] Cytec Thornel datasheet. viewed 17.10.2011 on www.matweb.com/search/.

- [15] DuPont. viewed 17.10.2011 on www2.dupont.com/Kevlar/.
- [16] Scheme of a pultrusion line. viewed 24.10.2011 on <http://industrialextrusionmachinery.com/>.
- [17] Choi, D. *Tensile behaviour of carbon fibre–glass fibre hybridized composites*. fib Symposium in Prague, (2011).
- [18] Sumida, A. *Heat resistance of continuous fibre reinforced plastic rods*, volume Fibre-reinforced plastics for reinforced concrete structures. University of Cambridge, (2001).
- [19] Ceroni, F. *Durability issues of FRP rebars in reinforced concrete members*. Cement and Concrete Composites, (2006).
- [20] Micelli, F. *Durability of FRP rods for concrete structures*. Construction and Building Materials, (2004).
- [21] Laoubi, K. *Creep and durability of sand-coated glass FRP bars in concrete elements under freeze/thaw cycling and sustained loads*. Cement and Concrete Composites, (2006).
- [22] Burgoyne, C. *Fibre reinforced polymers – strengths, weaknesses, opportunities and threads*. FRPRCS-9, (2009).
- [23] Subramaniam, K., Ghosn, M., and Ali-Ahmad, M. In *Advances in Construction Materials 2007*, Grosse, C. U., editor. Springer Berlin Heidelberg (2007).
- [24] Davalos, J. *Effect of FRP bar degradation on interface bond with high strength concrete*. Cement and Concrete Composites, (2008).
- [25] Shi, J. *Effects of freeze/thaw cycling and sustained load on FRP–concrete interface*. American Concrete Institute – Special publication, (2011).
- [26] Laš, V. *Mechanika kompozitních materiálů*. Západočeská univerzita v Plzni, (2008).
- [27] Halpin, J.C. and Kardos, J.L. *The Halpin–Tsai Equations: A Review*. Polymer engineering and science, (1976).
- [28] Halpin, J.C. and Tsai, S.W. *Effect of environment factors on composite materials*. Air Force tech. rep. AFML-TR-67-423, (1969).
- [29] Hewitt, R.L. and Malherbe, M.D.De. *An approximation for the longitudinal shear modulus of continuous fiber composites*. Journal of Composite Materials, (1970).

- [30] Eshelby, J. D. *The determination of the elastic field of an ellipsoidal inclusion and related problems*. Proceedings of the Royal Society of London, (1957).
- [31] Klusemann, B. *Homogenization methods for multi-phase elastic composites: Comparisons and benchmarks*. Otto-von-Guericke-Universitaet Magdeburg, (2010).
- [32] Hlobil, M. *Lecture notes on a subject: Composite materials*. Czech Technical University in Prague, (2010).
- [33] Černý, R. *Řešení transportních jevů na počítači*. Vydavatelství ČVUT, (1997).
- [34] Fish, J. and Belytschko, T. *A First Course in Finite Elements*. John Wiley & Sons, Ltd, (2007).
- [35] Červenka, V. et. al. *ATENA Program Documentation – Theory*. Cervenka Consulting Ltd., (2010).
- [36] ANSYS guide. viewed 10.12.2011 on www.kxcad.net/ansys/ANSYS/ansyshelp/.
- [37] ČSN EN 12390-3. *Zkoušení ztvrdlého betonu – část 3: Pevnost v tlaku zkušebních těles*. Český normalizační institut, (2002).